

# Comparisons of predicted bore evolutions by the Benjamin-Davis-Ono and Navier-Stokes equations for idealized mesopause thermal ducts

B. Laughman,<sup>1</sup> D. C. Fritts,<sup>1</sup> and J. Werne<sup>1</sup>

Received 26 April 2010; revised 9 September 2010; accepted 16 November 2010; published 27 January 2011.

[1] Numerical simulations are performed employing two numerical models to contrast nonlinear bore evolutions predicted by the Benjamin-Davis-Ono (BDO) equation with evolutions described by the Navier-Stokes (NS) equations. The first model is a simple one-dimensional solver of the BDO equation; the second describes the nonlinear two-dimensional dynamics of the NS equations. Both utilize the Boussinesq approximation. Owing to their simpler, horizontally isotropic nature, only isolated thermal ducts are considered in this study. Simulations assume an initial long-wave perturbation and address the influences of perturbation amplitude and wavelength, viscosity, and nonzero background stability on the resulting evolutions. Results indicate that the BDO equation provides reasonable predictions of bore character and evolution for conditions that satisfy its underlying assumptions. BDO predictions fail to describe bore character and evolution in cases where either the initial perturbations or the thermal environment differs significantly from BDO assumptions. Predictions employing the NS equations will thus provide more realistic guidance in the interpretation and understanding of bores observed in the mesopause region for general environments.

**Citation:** Laughman, B., D. C. Fritts, and J. Werne (2011), Comparisons of predicted bore evolutions by the Benjamin-Davis-Ono and Navier-Stokes equations for idealized mesopause thermal ducts, *J. Geophys. Res.*, *116*, D02120, doi:10.1029/2010JD014409.

## 1. Introduction

[2] For the past decade there has been a continuing effort to explain mesospheric bore observations. These efforts began when *Dewan and Picard* [1998] applied hydraulic theory to apparent observations of bores in the mesosphere and lower thermosphere (MLT), providing a qualitative starting point for understanding these phenomena. *Dewan and Picard* [2001] furthered these efforts by examining potential forcing mechanisms with scales relevant to MLT bore observations. Subsequent numerical studies performed by *Seyler* [2005] and *Laughman et al.* [2009] demonstrated the viability of numerical models employing the Navier-Stokes (NS) equations to generate bore-like evolutions from initial long-wave perturbations.

[3] The general study of solitons and bores in fluids has a much longer history, dating back to work done by *Airy* [1845], *Rayleigh* [1908], and *Lamb* [1932]. The Korteweg-de Vries (KdV) equation was the first clear and concise description of the balance between nonlinear steepening and dispersion which supports the existence of solitons, waves of permanent form [*Korteweg and de Vries*, 1895]. While this theory is an excellent approximation for surface waves,

it is less applicable to fluids with continuous density gradients. Internal solitary waves are better described by the Benjamin-Davis-Ono (BDO) equation and indeed this equation has provided guidance in studies of tropospheric bores such as the Morning Glory in Australia [*Christie*, 1989; *Porter and Smyth*, 2002].

[4] The goal of this paper is not to engage in an in-depth exposition of the KdV equation, the BDO equation, or their relative similarities and differences, though we will touch on a few points of each. A wealth of literature already exists detailing the characteristics of each, including, but not limited to, work by *Ono* [1975], *Koop and Butler* [1981], *Grimshaw* [1980], *Christie* [1989], and others [*Hammack and Segur*, 1974], whom we reference in section 2.

[5] Rather, the goal of this work is to address the conditions under which the BDO equation offers a good approximation to solutions of the NS equations in idealized environments and to explore the differences that arise when less idealized environments are considered, specifically a nonzero background stability and the effects of viscosity. It should be noted that the BDO equation has been extended to include viscous effects, compressibility effects, and radiative effects due to more complicated environments than those first considered by *Benjamin* [1967] [e.g., *Grimshaw*, 1980; *Maslowe and Redekopp*, 1980]. Our comparison studies make use of only the simple BDO equation and our study of nonidealized environments is confined to use of our 2-D NS model.

<sup>1</sup>CoRA Division, NorthWest Research Associates, Boulder, Colorado, USA.

[6] We discuss the KdV and BDO equations in section 2. Section 3 describes the numerical BDO and NS models used for these studies, including our nondimensionalization. Section 4 presents and contrasts the results of our BDO solutions with those of the NS equation for a variety of initial long-wavelength scales and amplitudes. Also presented are results of our NS model assuming finite viscosity and nonzero background stabilities. A discussion of our results and our conclusions are provided in section 5. Appendix A contains additional details about the BDO theory presented in section 2.2.

## 2. KdV and BDO Equations

[7] While the focus of this study is the comparison of bore evolutions predicted by the BDO and NS equations for varying initial conditions and environments, it is useful to first discuss the KdV equation. KdV theory is qualitatively similar to BDO theory and consists of a simpler formulation.

### 2.1. Korteweg–de Vries Equation

[8] The KdV equation is a finite amplitude “fairly long” (i.e., weakly dispersive) wave approximation for surface wave motion in a 2-D channel flow. The fluid density is assumed to be constant while the density of the overriding fluid (typically air) is assumed to be zero. Typical flow parameters include the undisturbed fluid depth,  $H$ , and the perturbation of the free surface from its undisturbed level,  $\eta(x, t)$ . Because the wavelengths considered are fairly long, the dispersion relation is not constant and takes the form

$$c = c_0(1 - \beta k^2). \quad (1)$$

For surface water waves, the long-wave phase speed is  $c_0 = (gH)^{1/2}$  and  $\beta = 1/6 H^2$  [Benjamin, 1967; Miles, 1981], and the wave number is  $k = 2\pi/\lambda$ . The dimensional form of the KdV equation is then [Hammack and Segur, 1974]

$$\frac{\partial \eta}{\partial t} + c_0 \frac{\partial \eta}{\partial x} + \frac{3}{2} \frac{c_0}{H} \eta \frac{\partial \eta}{\partial x} + \frac{1}{6} c_0 H^2 \frac{\partial^3 \eta}{\partial x^3} = 0. \quad (2)$$

The coefficient of the nonlinear term is  $3/2 c_0/H$  and the coefficient of the linear dispersion term is  $1/6 c_0 H^2$ . The competing effects of nonlinearity and dispersion are central to KdV and BDO theory.

[9] The KdV equation has stationary solutions, waves of permanent form, which represent a balance of dispersive and nonlinear effects. These solutions include periodic cnoidal waves (which we do not consider) and solitons of the form

$$\eta(x, t) = \eta_0 \operatorname{sech}^2 \left\{ (x - c_b t) \sqrt{\frac{3\eta_0}{4H^3}} \right\}, \quad (3)$$

where the KdV soliton velocity,  $c_b$ , is greater than the long-wave phase speed,  $c_0$ , and is given by

$$c_b = c_0(1 + \eta_0/2H). \quad (4)$$

For the KdV equation, the balance between nonlinear steepening (proportional to  $\eta_0/H$ ) and linear dispersion

(proportional to  $H^2/\lambda^2$  as seen in the dispersion relation) can be quantified by the parameter  $\lambda^2/H^3$ . Following Lighthill's [1978] treatment, if one regards the amplitude of a soliton to be half its height,  $a = 1/2\eta_0$ , and its “wavelength” to be the range over which the height is greater than some percentage of its maximum value, say 3%,

$$\lambda = 2 \left[ \operatorname{ArcSech}(\sqrt{0.03}) \right] \sqrt{\frac{4H^3}{3\eta_0}}, \quad (5)$$

then we obtain a value of  $\lambda^2/H^3 = 16.14 \sim 16$ . It is noteworthy that for solitons of any geometry this parameter's value is independent of  $H$ ,  $\lambda$ , and  $\eta_0$ . If one wishes to instead regard the “wavelength” to be only the square root term in equation (5) and the amplitude to simply be  $a = \eta_0$  then  $\lambda^2/H^3 = 1.333 \sim 1$ , indicating the relatively equal strengths of dispersive and steepening effects. For the remainder of this paper we will denote amplitude as  $\eta_0$ .

[10] Finally, it should be noted that due to the way it is derived, any initial perturbation that evolves according to the KdV equation will propagate preferentially in one direction, with the nonlinear evolution proceeding one direction and a possible dispersive component proceeding in the other in a frame moving with speed  $c_0$  [Benjamin, 1967].

### 2.2. Benjamin-Davis-Ono Equation

[11] The development of the BDO equation is qualitatively similar to that of the KdV equation. Fairly long waves of small but finite amplitude are considered and the result is an equation which contains competing dispersion and nonlinear steepening terms, and which has a soliton solution. However, whereas the KdV equation was derived for surface waves and evolves the surface displacement  $\eta(x, t)$ , the BDO equation is valid for internal waves present in a deep, density stratified fluid and evolves the displacement of the fluid throughout its vertical extent, which we denote  $\eta(x, z, t)$ . Examples of density profiles first considered in the development of BDO theory are described by equation (A3) and depicted in Figure 1 [Benjamin, 1967; Davis and Arcivos, 1967]. Figure 1a shows the density profile applicable to mesospheric bore modeling, while Figure 1b shows the profile similar to what we actually model. Under assumptions of vertical antisymmetry and the Boussinesq approximation, the two profiles have the same dynamics. In both, the length  $h$  is defined as the vertical range over which the density is variable.  $\rho_1$  and  $\rho_2$  are arbitrary constant densities and the mean density,  $\bar{\rho}_0$ , is equal to the density at  $z = 0$ , again due to antisymmetry.

[12] Associated with each density profile is a corresponding stability profile,

$$N^2(z) = \frac{g}{\bar{\theta}_0} \frac{d\theta_0(z)}{dz} = -\frac{g}{\bar{\rho}_0} \frac{d\rho_0(z)}{dz}, \quad (6)$$

where  $N^2$  is the buoyancy frequency squared,  $g$  is acceleration due to gravity,  $\rho_0(z)$  is the unperturbed density profile,  $\theta_0(z)$  is the unperturbed potential temperature profile, and  $\bar{\rho}_0$  and  $\bar{\theta}_0$  are the mean values of the density and potential temperature profiles. The equivalence of  $\theta_0(z)$  and  $\rho_0(z)$  defined by equation (6), as well as the use of  $\bar{\theta}_0$  and  $\bar{\rho}_0$  in place of  $\theta_0(z)$  and  $\rho_0(z)$  is valid under the Boussinesq

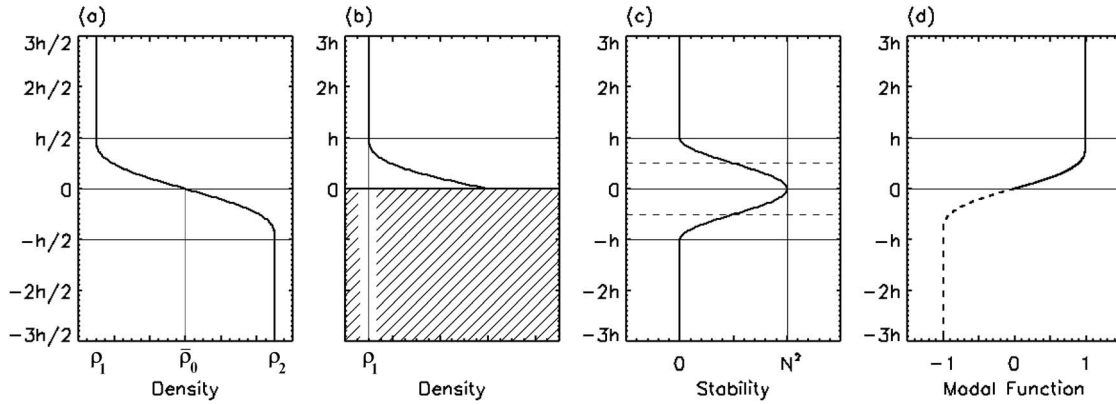


**Figure 1.** (a, b) Density profiles considered by the BDO equation. (c) Raised cosine stability profile used in our models. The dashed lines of Figure 1c mark the FWHM of the cosine duct from  $-h/2$  to  $h/2$ . (d) Modal function for the cosine stability profile computed for  $z \geq 0$  (solid line) and antisymmetrically reflected to the region  $z < 0$  (dashed line).

approximation where variations of  $\theta_0(z)$  and  $\rho_0(z)$  about their mean values are small. It should be noted that mesospheric bore dynamics can be on the order of a scale height, and consequently the results reported in this paper must be applied to observation with caution. The comparison of the BDO model with the NS results is unaffected, however, as both make the Boussinesq approximation. Figure 1c shows a stability profile which corresponds to the density profile in Figure 1a, though with the length scale doubled in order to make use of Figure 1b, vertical antisymmetry about  $z = 0$ , and the Boussinesq approximation for our comparison studies. Figure 1d displays the modal function,  $\phi(z)$ , associated with the  $N^2(z)$  profile in Figure 1c and will be discussed further below.

[13] The displacement,  $\eta(x, z, t)$ , can be separated into two functions: a horizontally dependent function that evolves in time and a time-independent modal function that varies with the vertical coordinate [Ono, 1975; Christie, 1989],

$$\eta(x, z, t) = A(x, t) \phi(z). \quad (7)$$

The modal function,  $\phi(z)$ , and the long-wave phase speed,  $c_0$ , both depend on the specific form of  $N^2(z)$  being considered (see Appendix A for details). The dispersion relation for “fairly long” internal waves is

$$c = c_0(1 - \gamma|k|), \quad (8)$$

where  $\gamma$  is a constant that depends on the specific density profile being considered. This contrasts with the dispersion relationship for surface waves (equation (1)) and unsurprisingly yields an evolution equation with a different dispersion term than the KdV equation,

$$\frac{\partial A}{\partial t} + c_0 \frac{\partial A}{\partial x} + \alpha A \frac{\partial A}{\partial x} + \delta \frac{\partial^2}{\partial x^2} H(A) = 0. \quad (9)$$

Here,  $H(A)$  is the Hilbert transform of  $A$ ,  $c_0$  is the long-wave phase speed, and the coefficients of the nonlinear term,  $\alpha$ , and the dispersion term,  $\delta$ , are functions of  $c_0$  and  $\phi(z)$  (see Appendix A for further details).

[14] Stationary solutions of the BDO equation are solitons. However, unlike the soliton solutions of the KdV equation, the solitons of the BDO equation are algebraic in nature, taking on the form

$$A(x, t) = \frac{\eta_0 \lambda^2}{(x - c_b t)^2 + \lambda^2}. \quad (10)$$

By inspection,  $\lambda$  is the half width at half maximum (HWHM) of the BDO soliton. The velocity is given by

$$c_b = c_0 + \frac{1}{4} \eta_0 \alpha = c_0 + \frac{\delta}{\lambda} \quad (11)$$

and demonstrates the same qualitative relationship between soliton velocity, soliton height, and soliton width as the KdV soliton: as the soliton width shrinks its amplitude and velocity both increase. Also, as with the KdV soliton, the BDO soliton has a speed greater than the linear long-wave phase speed  $c_0$ .

[15] The difference in the dispersion characteristics between the BDO and KdV equations also implies a different nondimensional parameter governing the relative strengths of dispersion and nonlinearity; in the case of the BDO equation the parameter is not  $\eta_0 \lambda^2 / H^3$ , where  $H$  is the depth of the fluid, but rather  $\eta_0 \lambda / h^2$ , where  $h$  is the interface thickness defined above and in Figure 1. To illustrate this difference consider a  $\text{sech}^2$  stability profile,  $N^2(z) = N_0^2 \text{sech}^2(z/h)$ , for which the value of  $\eta_0 \lambda / h^2$  is found to be 2.5. As with the KdV soliton, this parameter is independent of  $\eta_0$ ,  $h$ , and  $\lambda$  for an arbitrary soliton and is of order  $\sim 1$ . By contrast, computing the KdV parameter as  $\eta_0 \lambda^2 / h^3$  for the BDO soliton results in a function of  $\lambda/h$ , which contradicts the notion that solitons of *any* geometry represent the balance between nonlinearity and dispersion. Furthermore, the KdV value of 1.333 for a soliton would be obtained with  $\lambda/h = 0.5333$  while the BDO value of 2.5 would require  $\lambda/h = 1.0$ , both of which clearly violate the assumptions of both theories that  $\lambda > h$ .

[16] An important point to consider is that while the parameter  $\eta_0 \lambda / h^2$  is constant for arbitrary geometries of

BDO solitons, it is a function of the density profile. By inspection of equation (11),  $\eta_0\lambda = 4\delta/\alpha$ , implying that different ducting structures with different values of  $\delta$  and  $\alpha$  support different relative strengths of linear dispersion and nonlinear steepening behavior.

### 3. Numerical Models

[17] Two numerical models are employed in this study. The first is a NS model described in section 3.1; the second is a BDO model described in section 3.2. Both make use of the time stepping formulation and FFT routines described in section 3.1. In order to directly compare the results of each model, both use the same raised cosine stability profile depicted in Figure 1c and defined by equation (12), and both models are nondimensionalized by the full width at half maximum (FWHM) of  $h$  and peak stability  $N_0^2$ :

$$N^2(z) = \begin{cases} N_0^2 \left(\frac{1}{2}\right) [1 + \cos(\pi z/h)], & |z| \leq h \\ 0, & |z| > h \end{cases} \quad (12)$$

The cosine duct has the particular advantage that the relevant length scale for the BDO model,  $h$  in Figure 1b, and the chosen length scale for our NS model, the FWHM, is the same.

#### 3.1. Navier-Stokes Solver

[18] Our NS studies employ a numerical code solving the incompressible Boussinesq Navier-Stokes equations for direct numerical simulations (DNS) of bore generation and morphology assumed to occur in two spatial dimensions. Previous applications of this code have described 2-D bore studies [Laughman *et al.*, 2009] and three-dimensional (3-D) studies of nonlinear dynamics, turbulence transitions, and turbulence evolutions and statistics for both stratified shear flow (Kelvin-Helmholtz) instability, or KHI, and gravity wave breaking [see *Werne and Fritts*, 1999, 2001; *Fritts et al.*, 2003, 2006, 2009a, 2009b]. The code employs a pseudo-spectral solver that computes the nonlinear advection terms in physical space. Linear terms and derivatives are handled in Fourier space, and transformations between physical and Fourier space are performed by high-radix FFTs. Incompressibility (equation (14c)) is enforced via a two-stream function formulation expressed as

$$\vec{u} = \vec{\nabla} \times \vec{\psi} + \vec{\nabla} \times \vec{\nabla} \times \vec{\phi} + \vec{U}_0, \quad (13)$$

where the stream functions  $\vec{\psi} = (0, 0, \psi(x, y, z))$  and  $\vec{\phi} = (0, 0, \phi(x, y, z))$  are defined by the vertical velocity and the vertical vorticity fields and  $\vec{U}_0 = (U_0, V_0, 0)$  is the mean horizontal velocity [Fritts *et al.*, 2009a]. Potential temperature and the two stream functions are advanced in time with a third-order Runge-Kutta (RK) scheme [Spalart *et al.*, 1991]. The velocity and vorticity fields are computed from these quantities after each RK time substep according to equation (13). The time step is allowed to vary dynamically according to a Courant-Friedrichs-Lewy (CFL) condition of 0.68.

[19] The equations being solved are the incompressible Navier-Stokes equations subject to the Boussinesq approximation:

$$\partial_t \vec{u} + (\vec{u} \cdot \vec{\nabla}) \vec{u} = \nu \nabla^2 \vec{u} - \vec{\nabla}(P/\bar{\rho}_0) + (\rho/\bar{\rho}_0) \vec{g}, \quad (14a)$$

$$\partial_t \theta + (\vec{u} \cdot \vec{\nabla}) \theta = \kappa \nabla^2 \theta, \quad (14b)$$

$$\vec{\nabla} \cdot \vec{u} = 0, \quad (14c)$$

$$\rho = \bar{\rho}_0 [1 - \alpha(\theta - \bar{\theta}_0)], \quad (14d)$$

where  $\theta - \bar{\theta}_0$  is small. Equation (14) supports waves governed by the 2-D dispersion relation,

$$m^2 = \frac{N^2}{(U_0 - c)^2} - \frac{\partial^2 U_0 / \partial z^2}{(U_0 - c)} - k^2. \quad (15)$$

Here  $\mathbf{u} = (U_0 + \mathbf{u}, V_0 + \mathbf{v}, w)$  is the full 3-D velocity field,  $P$  is the pressure field,  $\rho$  is the density,  $\theta$  is the potential temperature, and  $\mathbf{g}$  is gravity. For the results presented in this paper  $U_0$  is always 0, as are  $\mathbf{v}$  and  $V_0$ .  $N^2$  is the buoyancy frequency defined by equation (6),  $k = 2\pi/\lambda_x$  and  $m = 2\pi/\lambda_z$ ,  $\lambda_x$  and  $\lambda_z$  are horizontal and vertical wavelengths, and  $\nu$  and  $\kappa$  are kinematic viscosity and thermal diffusivity, and  $\alpha$  is related to the coefficient of thermal expansion and is equal to  $1/\bar{\theta}_0$ .

[20] The length scale by which we nondimensionalize is chosen to be the FWHM of our stability duct, and our time scale is chosen to be  $1/N_0$ , where the peak stability is given by  $N_0 = (|\mathbf{g}| \alpha \beta)^{1/2}$ , where  $\beta$  is the magnitude of the maximum value of the vertical derivative of the potential temperature profile. These length and time scales define the velocity scale as  $u_0 = N_0 h$ . The Richardson number is then  $Ri = N_0^2 h^2 / u_0^2 = 1$ . We set  $\nu = \kappa$ , resulting in a Prandtl number  $Pr = 1$ , and so both the Reynolds and Peclet numbers are defined as  $Pe = Re = N_0 h^2 / \nu$ . According to equation (6), which employs the Boussinesq approximation, potential temperature is proportional to the vertical integral of the  $N^2$  profile and scales according to  $N_0^2 h$ . Units of temperature are recovered though the constants  $\mathbf{g}$  and  $\alpha$ , which for environments appropriate to the mesopause have values of  $9.55 \text{ ms}^{-2}$  and  $1/(8500 \text{ K})$ , respectively. With a chosen length scale of 5 km and a stability maximum  $N_0 = 0.0523599 \text{ s}^{-1}$ , our time scale is  $\sim 19 \text{ s}$  and our velocity scale is  $\sim 262 \text{ ms}^{-1}$ . We select a Reynolds number of 13090.0, corresponding to a kinematic viscosity of  $100 \text{ m}^2 \text{ s}^{-1}$ . For effectively inviscid runs viscosity is set to the vanishingly small value of  $10^{-4} \text{ m}^2 \text{ s}^{-1}$  resulting in a Reynolds number of  $1.309 \times 10^{10}$ ; this value was chosen because preliminary simulations performed with larger Reynolds numbers were not noticeably different from the  $10^{10}$  case. For all the effectively inviscid runs there is a limit on how long the simulation can run until the growing undamped Gibbs noise attains an amplitude comparable to the modeled dynamics [Laughman, 2009].

[21] All NS simulations presented in this paper assumed 2-D nonlinear dynamics and a domain having periodic horizontal boundary conditions and reflective upper and lower boundaries. Unless otherwise noted, all simulations also employ 1000 spectral modes in the horizontal and 2501

modes in the vertical. Specific horizontal domain sizes,  $x_{\max}$ , vertical domain sizes,  $z_{\max}$ , and numbers of grid points are given in section 4.

[22] Initializing the NS model consists of defining the mean environment and the perturbation to that environment. In every run the mean wind is set to zero while the nondimensional mean potential temperature profile in the region  $|z| < 1$  is given by equation (16a). Equation (16b) is the corresponding stability profile:

$$\bar{\theta}(z) = N_B^2 z + \frac{1}{2} (1 - N_B^2) \left[ z + \frac{1}{\pi} \sin(\pi z) \right], \quad (16a)$$

$$N^2(z) = N_B^2 + \frac{1}{2} (1 - N_B^2) [1 + \cos(\pi z)]. \quad (16b)$$

$N_B^2$  is the constant, nondimensional background stability in the region  $|z| > 1$  and is set to zero for all comparison runs with the BDO equation. For the purposes of this paper, the terms ‘‘background’’ or ‘‘background stability’’ refer to this region away from the duct with  $|z| > 1$ . We note that our mean temperature and stability are continuous functions while the third derivative of temperature is discontinuous at  $z = \pm 1$ . This reduces the order of our solver to two.

[23] We initialize our NS runs on the basis of the predictions of the BDO equation for two types of perturbations, a soliton and a sinusoid. Our initialization is computed according to equation (A1) in the inner region and equation (A9) in the outer region. The vertical velocity is initialized as the partial time derivative of the fluid displacement. The temperature perturbation is computed numerically by applying  $\eta(x, z)$  to the temperature field, mapping  $T(x, z, t)$  to  $T(x, z + \eta, t)$ . Specifically, the value of the initial potential temperature at  $T(x, z + \eta(x, z, 0), 0)$  is set equal to the value of the undisturbed potential temperature profile,  $T(z)$ . For values of  $\eta$  where  $z + \eta$  does not lie directly on a grid point a linear interpolation between neighboring grid points is used to compute  $T(x, z + \eta, 0)$ . The initial horizontal velocity is computed numerically from the specified vertical velocity according to equation (13).

[24] The specific forms of the soliton and soliton-like initializations are

$$\eta(x, z) = \begin{cases} S \frac{\eta_0 \lambda^2}{x^2 + \lambda^2} \varphi(z), & |z| < 1 \\ S \frac{\eta_0 (\lambda + z - 1)^2}{x^2 + (\lambda + z - 1)^2} env(z), & z > 1 \\ -S \frac{\eta_0 (\lambda - z - 1)^2}{x^2 + (\lambda - z - 1)^2} env(z), & z < 1 \end{cases}, \quad (17a)$$

$$w(x, z) = \begin{cases} S 2c_b x \frac{\eta_0 \lambda^2}{[x^2 + \lambda^2]^2} \varphi(z), & |z| < 1 \\ S 2c_b x \frac{\eta_0 (\lambda + z - 1)^2}{[x^2 + (\lambda + z - 1)^2]^2} env(z), & z > 1 \\ -S 2c_b x \frac{\eta_0 (\lambda - z - 1)^2}{[x^2 + (\lambda - z - 1)^2]^2} env(z), & z < 1 \end{cases}, \quad (17b)$$

$$env(z) = \frac{1}{2} \left[ \tanh\left(z + \frac{z_{\max}}{4}\right) - \tanh\left(z - \frac{z_{\max}}{4}\right) \right], \quad (18)$$

where  $S$  modifies the amplitude of the perturbation.  $S = 1$  is the soliton case while  $S \neq 1$  defines the soliton-like cases. The sine wave initialization is given by

$$\eta(x, z) = \begin{cases} \eta_0 \sin\left(\frac{2\pi}{\lambda_x} x\right) \varphi(z), & |z| < 1 \\ \eta_0 \sin\left(\frac{2\pi}{\lambda_x} x\right) \exp\left\{\frac{-2\pi}{\lambda_x} |z - 1|\right\} env(z), & z > 1 \\ -\eta_0 \sin\left(\frac{2\pi}{\lambda_x} x\right) \exp\left\{\frac{-2\pi}{\lambda_x} |-z - 1|\right\} env(z), & z < 1 \end{cases}, \quad (19a)$$

$$w(x, z) = \begin{cases} \frac{-2\pi}{\lambda_x} \eta_0 c_0 \cos\left(\frac{2\pi}{\lambda_x} x\right) \varphi(z), & |z| < 1 \\ -\frac{2\pi}{\lambda_x} c_0 \eta_0 \cos\left(\frac{2\pi}{\lambda_x} x\right) \exp\left\{\frac{-2\pi}{\lambda_x} |z - 1|\right\} env(z), & z > 1 \\ \frac{2\pi}{\lambda_x} c_0 \eta_0 \cos\left(\frac{2\pi}{\lambda_x} x\right) \exp\left\{\frac{-2\pi}{\lambda_x} |-z - 1|\right\} env(z), & z < 1 \end{cases}. \quad (19b)$$

Since there is no relationship between  $\lambda$  and  $\eta_0$  for a sine wave, the variable  $S$  serves no purpose here; a value of  $S$  other than 1 is absorbed by the amplitude  $\eta_0$ . The purpose of the envelope function defined by equation (18) is to force the vertical velocity perturbation to a value of strictly zero at the upper and lower boundaries. The reason for this is that the spectral formulation of the code requires a vertical velocity of zero at these boundaries; failing to do so results in significant Gibbs oscillation. A number of simulations were performed to test the effect of this envelope on the resulting evolution, and the resulting choice of vertical domain size minimizes these effects without unduly sacrificing efficiency.

### 3.2. BDO Solver

[25] The numerical model used to solve the BDO equation is composed of two parts – the first solves the modal equation for  $\phi(z)$  and  $c_0$ , and determines the values of  $\alpha$  and  $\delta$ , and the second evolves the nondimensional equation (9).

[26] A fourth-order Runge-Kutta integration is used to solve equations (A5) and (A6) for nondimensional values of  $\alpha$ ,  $\delta$ ,  $c_0$ , and the modal function,  $\phi(z)$  from an initial stability profile,  $N^2(z)$ . For the cosine stability profile these values are  $\alpha = 1.03714$ ,  $\delta = 0.09318$ , and  $c_0 = 0.33715$ , with the corresponding modal function plotted in Figure 1d. Equation (A5) is solved in the region  $z \geq 0$  (denoted by the solid line) and then reflected antisymmetrically to the region  $z < 0$  (denoted by the dashed line). The parameter  $\eta_0 \lambda / h^2$  then has a value of 0.3594.

[27] In order to test the accuracy of these values, we numerically compute values for  $\alpha$ ,  $\delta$ , and  $c_0$  for the  $\text{sech}^2$  duct and compare them against their analytically obtained values. The results are presented in Table 1 and demonstrate very good agreement (within 0.04%), lending confidence to the values used for the cosine profile. For the  $\text{sech}^2$  duct we use 10,000 grid points over a nondimensional vertical domain from 0 to 100 to allow the stability to asymptote to

**Table 1.** Analytically and Numerically Obtained Values of  $\alpha$ ,  $\delta$ , and  $c_0$  for the Sech<sup>2</sup> Stability Profile

	Analytic Value	Numerical Value	Percent Difference
$\alpha$	0.848528	0.848276	0.0297
$\delta$	0.530330	0.530361	0.0057
$c_0$	0.707107	0.706842	0.0375

zero. For our cosine duct we use 10,000 grid points over a vertical range of 0 to 1 since including values of  $z > 1$  where the cosine stability profile is strictly zero does not change any of the obtained values.

[28] The horizontal time evolution is handled in the same manner as in the NS model described in section 3.1. The only difference is that instead of time evolving three, 3-D quantities,  $w(x, t)$ ,  $\theta(x, t)$ , and the vertical component of vorticity,  $\omega_z(x, t)$ , according to the NS equations, the BDO model evolves one, 1D quantity,  $A(x, t)$ , according to the BDO equation.

[29] Finally, in order to compare these results with those of our NS model we compute the displacement field throughout the vertical domain  $[-1, 1]$ . The Boussinesq approximation allows us to assume the dynamics predicted by the BDO equation are vertically antisymmetric about the center of the duct,  $z = 0$ , and so we compute the displace-

ment from equation (7) for  $z = [0, 1]$  and reflect it about the center of our domain. With our displacement known we compute the corresponding perturbation to the temperature field by mapping  $T(x, z, t)$  to  $T(x, z + \eta, t)$  in the region  $|z| < 1$ . Comparisons between the BDO and NS models consist of comparing the potential temperature fields and we do not compute the vertical velocity field for the BDO prediction.

#### 4. Results

[30] Sections 4.1–4.3 present the results of both models for soliton and sinusoidal initializations with a range of amplitudes and length scales under inviscid and strictly neutral background stability conditions. Section 4.1 utilizes the soliton initialization (equation (16) with  $S = 1$ ) while section 4.2 uses a soliton-like localized forcing ( $S \neq 1$ ). Section 4.3 utilizes an idealized sine wave initialization. Section 4.4 presents results from the NS model when viscosity is present, and section 4.5 details the effects of non-zero background stability.

[31] Unless otherwise noted all results are reported in a reference frame moving rightward with velocity  $c_0$ . Figures 2, 3, 4, and 6 use markers to track three velocities: the thin vertical line represents the origin in the moving frame and has a velocity  $c_0$  in the stationary frame. The diamonds

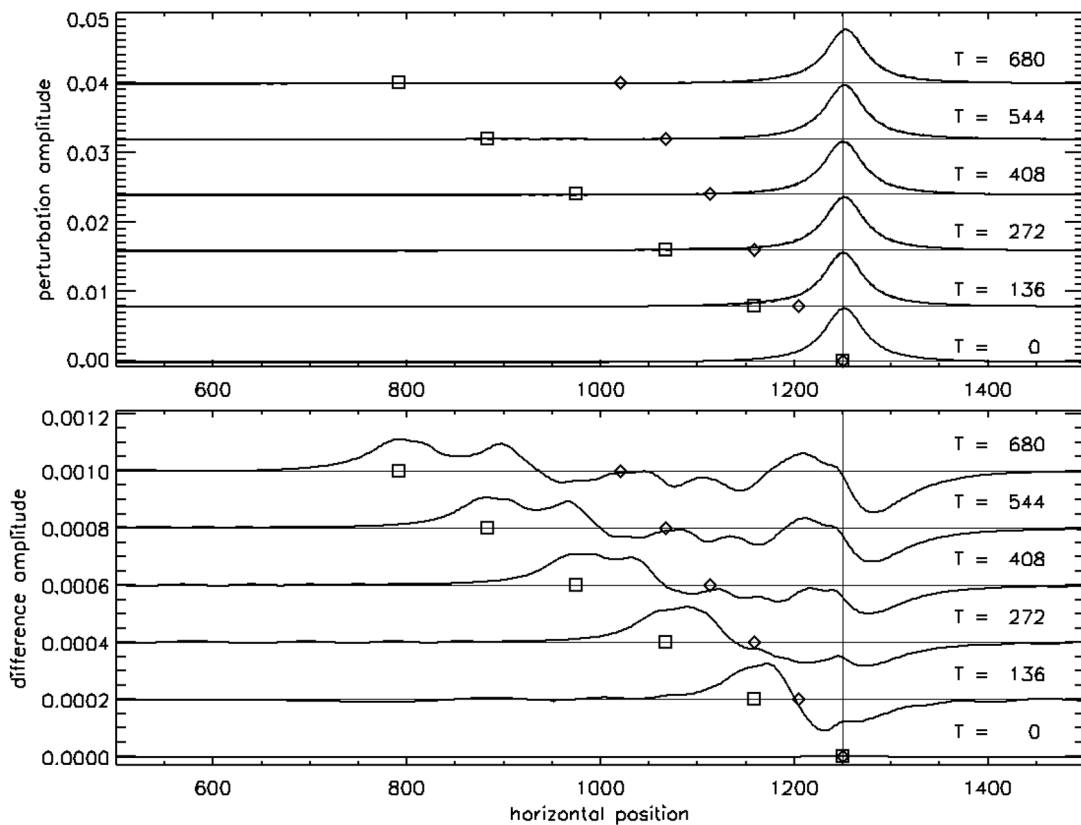


**Figure 2.** Time evolution of a  $\lambda = 4\delta/\alpha\eta_0 = 25$  soliton depicted in a reference frame moving with the long-wave phase speed  $c_0 = 0.33715$ . (top) The horizontally averaged potential temperature predicted by the NS (solid line) and BDO (dashed line) equations. (bottom) The difference between the NS and BDO solutions (NS minus BDO). The diamond moves leftward with velocity  $c_0$  and represents the origin in the stationary frame. The square moves leftward with velocity  $-2c_0$  and represents the point moving leftward with the long-wave phase speed in the stationary frame.

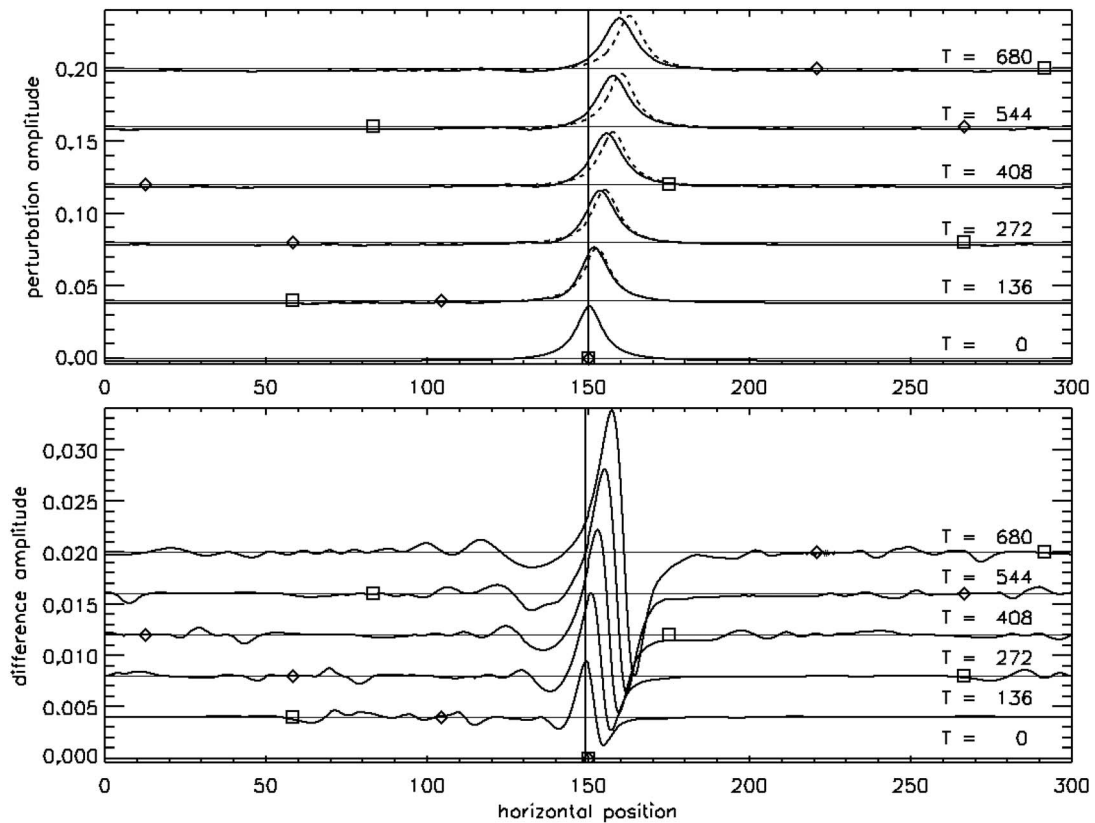


**Figure 3.** Time evolution of a  $\lambda = 5$  soliton depicted in a reference frame moving with the long-wave phase speed  $c_0 = 0.33715$ . (top) The horizontally averaged potential temperature predicted by the NS (solid line) and BDO (dashed line) equations. (bottom) The difference between the NS and BDO solutions (NS minus BDO).

move leftward with velocity  $-c_0$  and represent the origin in the stationary frame. The squares move leftward with velocity  $-2c_0$  and represent the point in the stationary frame moving leftward with velocity  $-c_0$ .

#### 4.1. Soliton Initialization

[32] The soliton initial condition is ideal for comparing the two models as it is the stationary solution predicted by BDO theory. The predicted evolution for each model should then be a strictly horizontal translation of the initial condition. Cases were run for wavelengths  $\lambda$  ranging from 100 to 0.1, with corresponding amplitudes defined by  $\eta_0 = 4\delta/\alpha\lambda$ .

[33] Figure 2 displays the results of the  $\lambda = 25$ ,  $\eta_0 = \sim 0.014$  soliton and is fairly representative of the behavior of solitons with  $\lambda \approx 10$  and larger. The horizontal domain size,  $x_{\max}$ , is 2500 with 1000 grid points and the vertical domain size,  $z_{\max}$ , is 50 with 2501 grid points. The first feature to note is that the bore velocity, given by equation (11), is very nearly equal to the long-wave phase speed and appears to be nearly stationary. The second noteworthy feature in Figure 2 is the close agreement between the NS and BDO models, with the largest amplitude difference between the two models at about 2.5% of the initial perturbation amplitude. This agreement is highlighted by the inability to distinguish the solid line of Figure 2 from the dashed line representing the BDO solution.

[34] The dispersive wave train that develops at  $x \sim 1250$  propagates leftward at the long-wave phase speed (tracking the squares) with an amplitude of about 1% that of the initial perturbation and represents dispersive effects not predicted by the BDO equation. This dispersive wave train owes its existence to the fact that an arbitrary forcing has the potential to excite a variety of different dynamical responses; the soliton forcing is “arbitrary” in the following two ways. The first is that the BDO equation is an approximation, and while its validity is better for the length scales it assumes, it is never a completely accurate representation of the physics being modeled. Because of this, while the soliton is an exact solution of the BDO equation, it cannot also be an exact solution of the NS equations. The emergent dispersive wave then represents motions that the BDO code fails to predict, and that the NS code describes fully.

[35] The second effect potentially contributing to this wave is the potential mismatch between the initial temperature and vertical velocity perturbations. The BDO equation is initialized with one quantity, displacement. The NS model, however, requires two fields. Extensive testing not presented here has shown that changing the relative magnitudes of the temperature and velocity perturbations can lead to significant departures from the BDO prediction, with the most striking example being the case of an initial temperature perturbation with no velocity perturbation. In this case the resulting motion was symmetric long-wave dis-

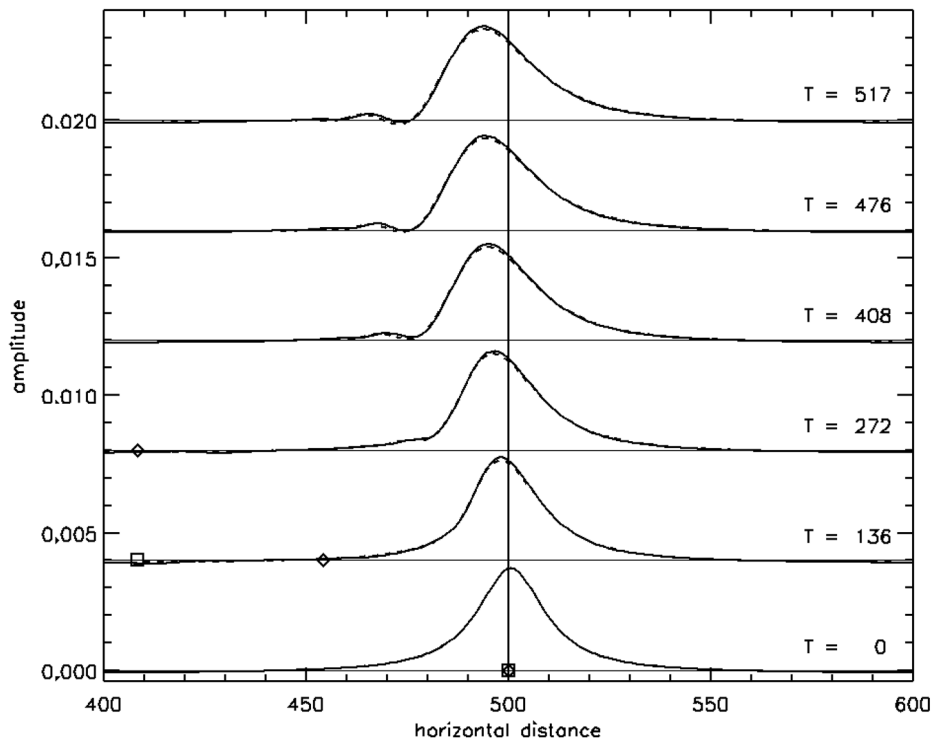


**Figure 4.** Time evolution of a  $\lambda = 10$ ,  $S = 0.2$  perturbation shown in a reference frame moving with the long-wave phase speed  $c_0 = 0.33715$ . Displayed are the horizontally averaged potential temperatures predicted by the NS (solid line) and BDO (dashed line) equations.

turbances propagating outward from the origin with velocity  $\pm c_0$ , qualitatively similar to the motion accompanying dropping a stone into a pond. No choice of relative amplitudes completely eliminated the dispersive wave, lending support to the first notion that this wave represents, in part at least, the limitations of the BDO equation.

[36] The final effect worth noting is the very small amplitude leftward traveling wave present at  $x = 770$ ,  $t = 136$ . This small-amplitude perturbation travels with a velocity of  $10c_0$  and is the result of the impermeable upper and lower boundaries. This simulation was run with vertical domain sizes of 16, 25, 33.3, 50, 66.67, and 100 and while the soliton and dispersive wave evolution remained unchanged, the velocity of this small-scale feature changed according to  $V_{\text{feature}} = \sqrt{2} c_0 (z_{\text{max}})^{1/2} \sim 0.47 (z_{\text{max}})^{1/2}$ , behavior which is qualitatively similar to that of long waves in shallow water theory. In addition to the BDO equation, Benjamin's [1967] paper also includes a discussion of a system of two immiscible fluids of different densities and depths bounded above and below by impermeable vertical boundaries. That analysis provides the long-wave phase speed of waves propagating along the interface between the two fluids, and in our notation with the interface vertically located in the middle of the domain the long-wave phase speed is  $c_{0,\text{interface}} = 0.5 (z_{\text{max}})^{1/2}$ , which is within 6% of our model's values. This 6% discrepancy is likely due to the fact that Benjamin's analysis assumed the interface to be a sharp density discontinuity while our model was run with a region of smoothly varying density (the duct). Furthermore, while the soliton evolution is vertically antisymmetric about the center of the duct, this long-wave feature is not, which supports the

interpretation that it is analogous to a surface wave propagating on the interface. This wave is a physical response to unphysical boundary conditions and in light of its small amplitude and apparent lack of influence on the main dynamics considered, we neglect its contribution from this point forward.

[37] For wavelengths smaller than 10, the two models begin to diverge more significantly. Results for  $\lambda = 5$  are depicted in Figure 3. The horizontal domain size is 300 with 3000 grid points and the vertical domain size is 50 with 2501 grid points. The increasingly narrower width of the initial perturbation further violates the assumptions of the BDO equation and the resulting evolution bears this out. The most noteworthy feature in Figure 3 is the dispersive wave train that forms at the origin and propagates leftward with velocity  $\sim c_0$ . The amplitude of this response is  $\sim 3\%$  of the initial perturbation, significantly larger than the dispersive wave of Figure 2. The growing strength of this dispersive component owes its existence to the fact that the BDO soliton is becoming a less accurate approximation for a steady solution of the NS equations for this short length scale (if, indeed, a truly steady solution to the NS equations exists at these scales). Consequently, the initial perturbation excites both a soliton like response and a stronger dispersive wave response.

[38] In addition to the growing strength of the dispersive wave, the two predicted evolutions of the BDO soliton begin to differ at this length scale. The NS-evolved soliton clearly lags the BDO prediction. It is no longer meaningful to discuss the amplitude difference between the NS and BDO solitons; they now propagate with different velocities and

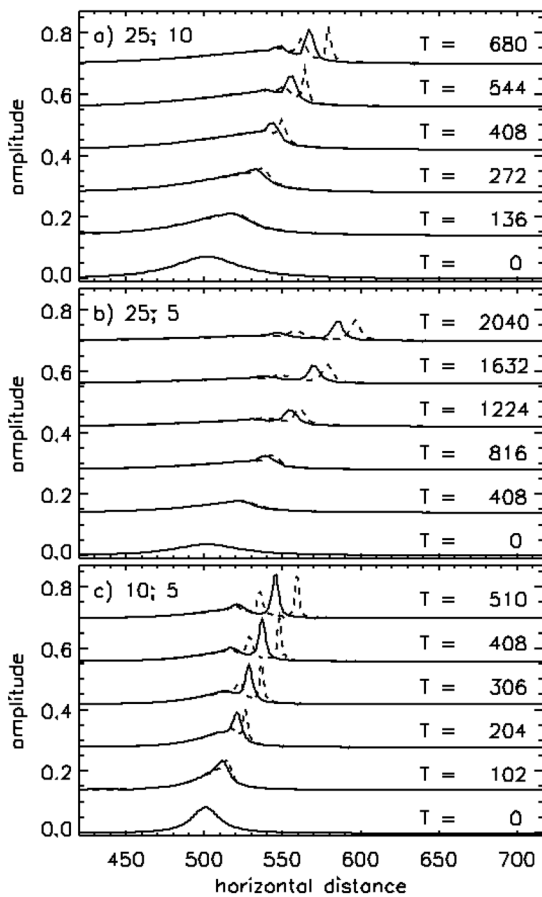


**Figure 5.** Time evolution of three soliton-like initial conditions defined by equation (16). Nondimensional times are listed above each trace. (a) The results of a  $\lambda = 25$ ,  $S = 10$  perturbation. (b) The results of a  $\lambda = 25$ ,  $S = 5$  perturbation. (c) The results of a  $\lambda = 10$ ,  $S = 5$  perturbation. Displayed are the horizontally averaged potential temperatures predicted by the NS (solid line) and BDO (dashed line) equations.

the leading peak of the difference plot merely highlights this.

[39] The  $\lambda = 1$  and  $\lambda = 0.5$  cases (not shown) represent the lowest values of  $\lambda$  for which the BDO model even qualitatively captures the behavior predicted by the BDO equation. The strength of the dispersive waves continues to grow in amplitude and the predicted soliton geometries and velocities disagree even more strongly for these wavelengths. It is nevertheless remarkable that the qualitative behavior exhibited by the NS solution, namely, the emergence of a soliton-like peak, is similar to that predicted by the BDO equation. It is especially remarkable that this qualitative behavior occurs for values of  $\lambda \leq h$  when the BDO equation is derived assuming  $\lambda \gg h$ . At the smallest value evaluated,  $\lambda = 0.1$ ,  $\eta_0 = \sim 3.5$ , the two models diverge wildly. The NS model predicts turbulent breaking while the BDO model, which is a weakly nonlinear theory unable to model such nonlinear features as recirculation regions or breaking, continues to predict horizontal translation of the initial condition. Also, as energy more readily accumulates at smaller scales in the absence of viscosity numerical noise begins to dominate the solution. The addition of viscosity

suppresses these small-scale motions, but also removes energy from the dynamics we wish to evaluate more quantitatively.

#### 4.2. Soliton-Like Initialization

[40] In this section we compare results obtained with the BDO and NS codes for a soliton-like initialization, where the value of  $S$  in equation (16) is different from 1. Again, a number of simulations were performed from which we present a few representative cases.

[41] The first case we consider is that of a reduced amplitude displayed in Figure 4, with  $\lambda = 10$  and  $S = 0.2$ , which is representative of all cases with  $S < 1.0$ , where both the NS and BDO solutions agree fairly well. The horizontal domain size is 1000 with 1000 grid points and the vertical domain size is 50 with 5001 grid points. There are two features to consider. The first is the leading peak, which according to both models has a velocity less than the long-wave phase speed. This result is to be expected, as the velocity of a soliton is proportional to its amplitude and since the soliton represents the balance between amplitude-dependent nonlinear effects and linear dispersion it follows that reducing the amplitude allows linear dispersion to dominate the perturbation's evolution. The dispersive character is also reflected in the shallow leading edge and the steepened trailing edge of the initial perturbation. The difference in amplitudes predicted by the two models for the  $S = 0.2$  case is  $\sim 1 \times 10^{-4}$ , roughly 2.5% of the peak amplitude of 0.004. For the  $S = 0.5$  case, the peak amplitude difference is  $\sim 2 \times 10^{-4}$ , roughly 2% of the peak amplitude of 0.01. The initial dispersive wave with velocity  $-c_0$  from section 4.1 is present as well with an amplitude of  $\sim 1\%$  the initial peak amplitude.

[42] The second feature we consider is the dispersive wave train trailing the leading peak. The dispersive waves that were seen to develop in Figures 2 and 3 were due to the growing effects of linear dispersion in the NS model due to shorter horizontal length scales of the initial perturbation, which violated the approximations of the BDO theory. Those dispersive waves were not predicted by the BDO equation. The dispersive tail forming in Figure 4, however, is the direct result of an initial perturbation with a decreased amplitude that favors dispersive effects over nonlinear effects, thus both the BDO and NS models predict this dispersion. Finally, we note that dispersive effects increase with decreasing values of  $S$  (not shown).

[43] Figure 5 displays the results for values of  $S > 1$ . Figure 5a displays the results of a  $\lambda = 25$ ,  $S = 10$  initial condition, Figure 5b shows the evolution of a  $\lambda = 25$ ,  $S = 5$  initial condition, and Figure 5c shows a  $\lambda = 10$ ,  $S = 5$  soliton-like perturbation. For the  $\lambda = 25$  cases, the horizontal domain size is 2500 with 1000 grid points and the vertical domain size is 50 with 2501 grid points. For the  $\lambda = 10$  case the horizontal domain size is 1000 with 1000 grid points and the vertical domain size is 50 with 5001 grid points. All are plotted with the same horizontal and vertical scale, with the nondimensional times of each trace listed above. These three cases can be contrasted with one another and reveal three trends. The first is that while none of the three cases display good agreement between the NS and BDO predictions, agreement between the two theories is best for smaller

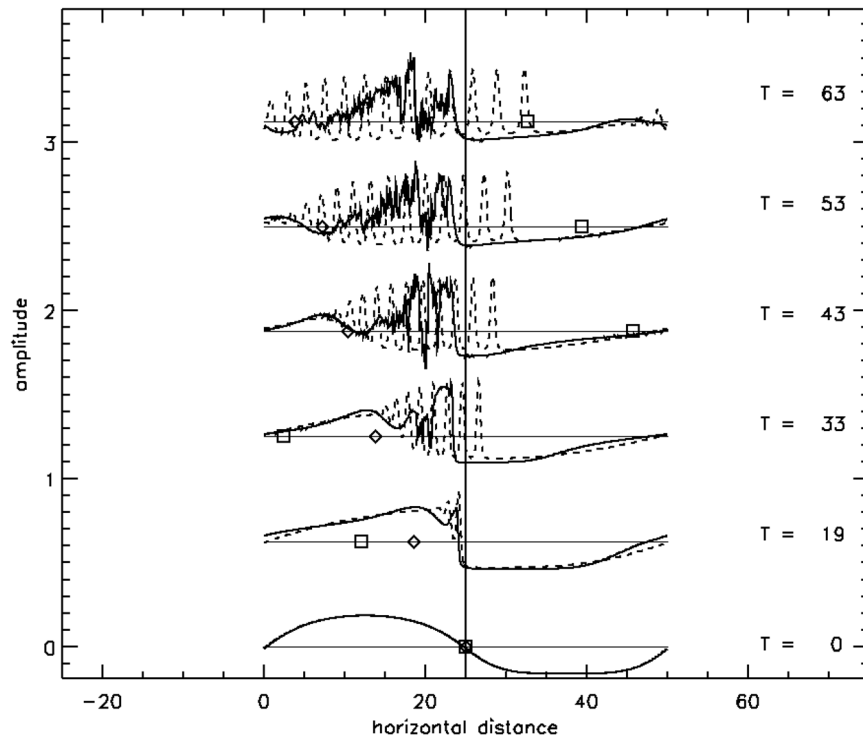


**Figure 6.** Time evolution of a  $\lambda = 50$ ,  $\eta_0 = 0.5$  sinusoidal perturbation. The solid line is the NS solution, and the dashed line is the BDO solution.

amplitudes, with the  $\lambda = 25$ ,  $S = 5$  case displaying better agreement than the other two.

[44] The second feature to note is that the time required for independent peaks to emerge from the initial condition is inversely dependent on amplitude, with the  $\lambda = 25$ ,  $S = 5$  case requiring almost three times as long as the  $\lambda = 25$ ,  $S = 10$  case to begin to develop independent peaks ( $T = 816$  of Figure 5b compared to  $T = 272$  of Figure 5a).

[45] The final noteworthy behavior is the dependence of this crest creation time on the wavelength. The  $\lambda = 10$ ,  $S = 5$  case develops peaks at about  $T = 102$ , which is a factor of 8 smaller than the crest creation time of the  $\lambda = 25$ ,  $S = 5$  case of  $T = 816$ . While this behavior may owe its existence more to the differences in amplitude between the  $\lambda = 10$  and  $\lambda = 25$  solitons than it does to the difference in width, it is worth recognizing that neither the  $\lambda = 25$ ,  $S = 1$  soliton nor the  $\lambda = 10$ ,  $S = 1$  soliton experiences crest separation, so interpreting the difference in width as resulting in a difference in separation time scale for the same pre-factor  $S = 5$  is reasonable.

### 4.3. Sinusoidal Initialization

#### 4.3.1. Large-Amplitude Sinusoid

[46] In this section we compare the responses predicted by the BDO and NS codes to initial sinusoidal perturbations described by equation (17), focusing on effects due to varying perturbation wavelengths and amplitudes. We begin by presenting the results of each model for a fairly large amplitude perturbation. Figure 6 shows the results of the  $\eta_0 = 0.5$ ,  $\lambda = 50$  case. The horizontal domain size is 50 with 1000 grid points and the vertical domain size is 100 with 2501 grid points. The results shown in Figure 6 are qualita-

tively similar to the other three cases run with  $\eta_0 = 0.5$ , namely those with  $\lambda = 20$ , 100, and 200.

[47] There are three noteworthy features in Figure 6. The first is that the 2-D NS result is quantitatively unreliable because the nonlinear response is very strong, rapidly cascades energy to small scales, and would also excite 3-D turbulent motions accompanying overturning if allowed to do so. Our assumption of nearly inviscid motions exacerbates of the numerical noise that arises at smaller scales. A second noteworthy feature is that, despite the problems present in the NS results, it nevertheless predicts nonlinear breaking for this large-amplitude wave. A third noteworthy feature highlights the limits of BDO equation applicability alluded to in section 4.1 and is the reason for discussing Figure 6. The BDO equation is a weakly nonlinear theory which predicts crest creation to account for all nonlinear effects. When initialized with a perturbation that leads to overturning and breaking behavior in the NS solution, the BDO response is simply crest creation. This underscores the inherent limits of the BDO equation for large initial perturbation amplitudes.

#### 4.3.2. Wavelength Variations

[48] Reducing the amplitude of the perturbation removes the strongly nonlinear tendencies from the response, such as closed circulations and breaking. Figure 7 displays the results of a  $\lambda = 100$ ,  $\eta_0 = 0.1$  perturbation (Figure 7a) and a  $\lambda = 200$ ,  $\eta_0 = 0.1$  perturbation (Figure 7b) plotted on the same horizontal scale. For  $\lambda = 100$  the horizontal domain size is 100 with 1000 grid points, while for  $\lambda = 200$  the horizontal domain size is 200 with 1000 grid points. Both have a vertical domain size of 100 with 2501 grid points.

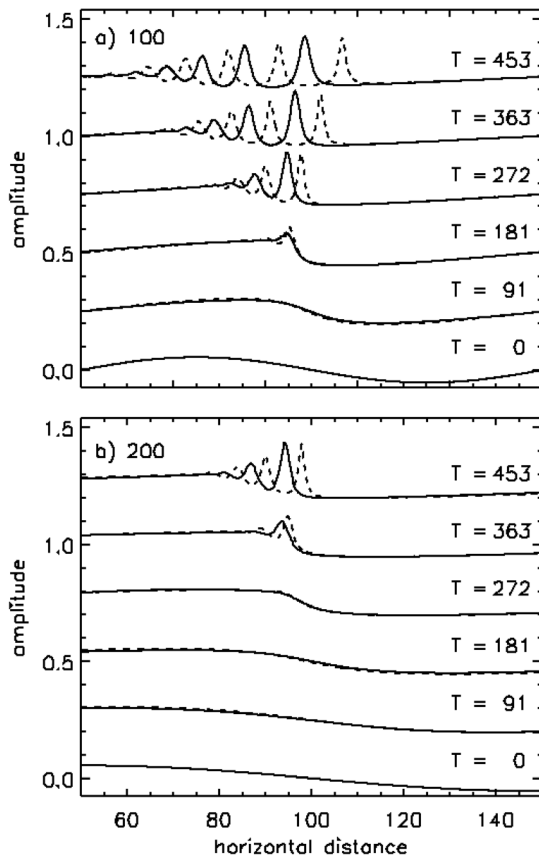


**Figure 7.** (a) Time evolution of a  $\lambda = 100$ ,  $\eta_0 = 0.1$  sinusoidal perturbation. (b) Time evolution of a  $\lambda = 200$ ,  $\eta_0 = 0.1$  sinusoidal perturbation. The solid line is the NS solution, and the dashed line is the BDO solution. Both horizontal and amplitude scales are the same.

Other wavelength considered with  $\eta_0 = 0.1$  include 50, 20, and 2.

[49] Figure 7 highlights five characteristics of the sinusoidal initialization. The first and most obvious is that both the NS and BDO solutions predict a series of amplitude-ordered crests, with the larger amplitude peaks leading the smaller. The second is that the NS and BDO results agree fairly well up to the point of crest creation, with both codes predicting roughly the same time for the initial crest emergence. A third characteristic highlighted by Figure 7 is that the time scale over which crests begin to emerge is dependent on the initial perturbation wavelength. Figure 7a shows a peak beginning to emerge at  $T = 181$ , while Figure 7b predicts a peak emergence at time  $T = 363$ , twice as long as the  $\lambda = 100$  case. This supports the interpretation in section 4.2 that the length scale plays a role determining the time scale over which individual peaks emerge.

[50] A fourth characteristic of the sinusoidal initialization is the relative independence of the emerging crests' geometries on the wavelength. For all perturbation wavelengths, the leading peak develops with a FWHM of  $\sim 2.5$  and an amplitude of  $\sim 0.25$ . This also explains why traces at  $T = 363$  and 453 of Figure 7b appear to be similar to traces at  $T = 181$  and 272 of Figure 7a; once the peaks emerge, their

dynamics are governed by their amplitudes and are no longer dependent on the initial perturbation.

[51] The final noteworthy feature of Figure 7 is that the BDO solution noticeably leads the NS prediction. One plausible explanation for this behavior is that since the BDO equation is an approximation that handles nonlinearity solely through crest creation, as in Figure 6, there are additional processes being modeled by the NS equations that may delay the onset of crest creation which the BDO equation fails to capture. Another plausible explanation is that the initial perturbation in the NS model is exciting a dispersive response in addition to the nonlinear response and that this leads to more slowly developing crests. While the exact reasons for this behavior are unknown, this result is consistent with the results presented in Figures 2, 3, and 5.

#### 4.3.3. Amplitude Variations

[52] Again, simulations were run with numerous combinations of  $\lambda$  and  $\eta_0$ . Figure 8 presents the results of a  $\lambda = 200$  wave with,  $\eta_0 = 0.1, 0.06, 0.03,$  and  $0.01$ . The horizontal domain size is 200 with 1000 grid points and the vertical domain size is 100 with 2501 grid points. Note that the horizontal scale plotted in Figure 8 is twice as large as that in Figure 7, and the vertical scale of Figure 8d is  $1/10$ th that of Figures 8a–8c.

[53] There are a few noteworthy features highlighted in Figure 8. The first is that as the amplitude of the initial perturbation decreases, the agreement between the NS and BDO results improves. A second is that as the amplitude of the initial perturbation decreases the emergence time of the initial crest increases in a very consistent manner: reducing the initial amplitude by a factor of 0.6 increases the emergence time by a factor of  $\sim 1/0.6 (= 1.667)$ , reducing the initial amplitude by a factor of 0.3 increases the emergence time by a factor of  $\sim 1/0.3 (= 3.333)$ , and reducing the initial amplitude by a factor of 10 increases the emergence time by a factor of  $\sim 8.5$ , though with the large time scales involved in Figure 8d it becomes more difficult to define the “crest creation” time. A third noteworthy feature seen in Figure 8 is that the geometry of the emerging peaks is strongly dependent on the perturbation amplitude. Unlike Figure 7, where the emergent peaks are relatively similar, there is a noticeable trend for smaller and broader peaks to emerge as the initial perturbation amplitude is decreased.

[54] Finally, the apparent sub- $c_0$  velocity of the leading peak of Figure 8d needs to be addressed. This behavior, with the leading emergent peak lagging the long-wave phase speed, was observed in a number of runs where the leading emergent peak had a width comparable to the initial perturbation wavelength. It is possible, though unconfirmed at the moment, that this behavior is due to the periodicity of the forcing. The horizontal domain is periodic, and so the evolution depicted in Figure 8 is really the evolution of a segment of an infinitely long wave train. It is reasonable to expect that the tail of the evolution, which is long relative to the horizontal domain, will wrap around and interact with the leading peak, and that the sum of these two effects is a peak which travels with velocity less than the long-wave phase speed. That both the NS and BDO models predict this behavior supports this notion, as does the fact that this behavior was seen for a variety of amplitudes and wavelengths when the emergent peak was of comparable width to the horizontal domain. Fully testing this would require

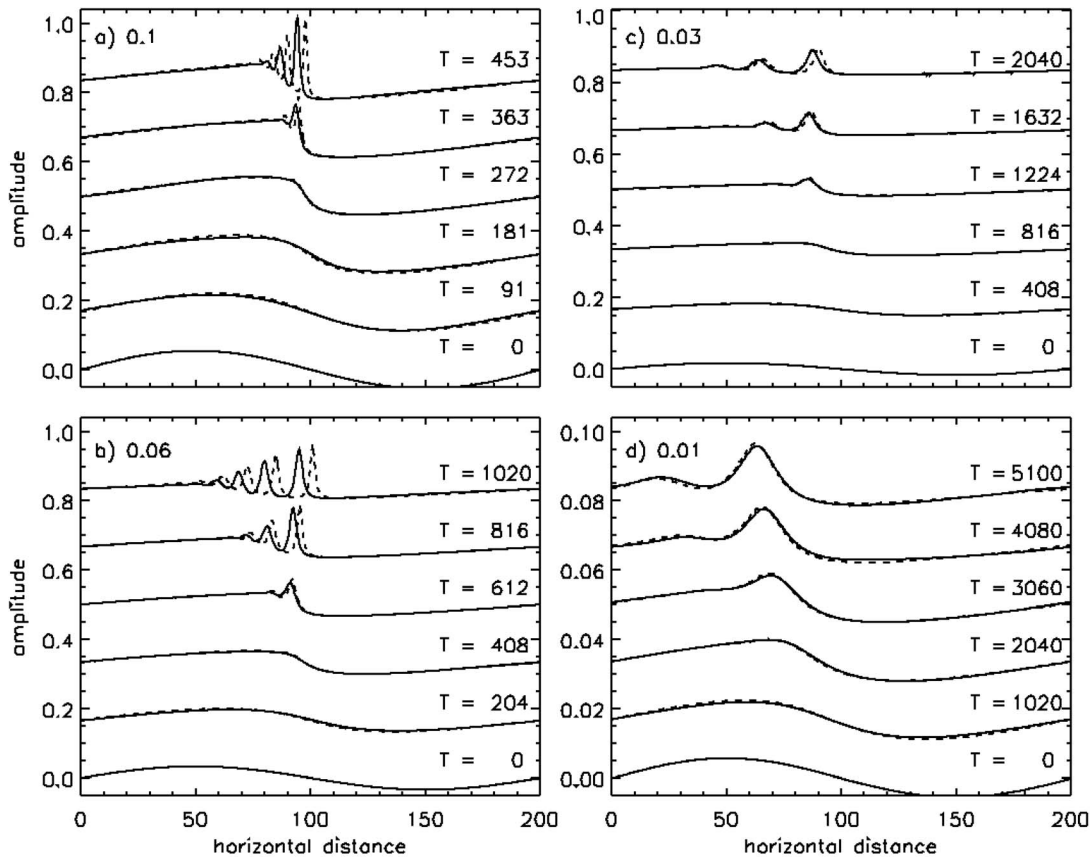


**Figure 8.** Time evolution of a  $\lambda = 200$  perturbation with amplitude (a)  $\eta_0 = 0.1$ , (b)  $\eta_0 = 0.06$ , (c)  $\eta_0 = 0.03$ , and (d)  $\eta_0 = 0.01$ . Note that the scale of Figure 8d is a factor of 10 smaller than that of Figures 8a–8c. The solid line is the NS solution, and the dashed line is the BDO solution.

initializing the model with an isolated sine wave, though the observed behavior might be expected for a real sine wave initialization allowing nonlinear evolutions at successive crests.

#### 4.4. Viscous Effects

[55] We considered the effects of viscosity for a variety of length scales and amplitudes for both sinusoidal and soliton-like initial conditions. The results were fairly uniform in the sense that every simulation exhibited the same general effects. Unsurprisingly, the addition of viscosity acted to remove energy from the response, as in Figure 9, which displays the results of a  $\lambda = 200$ ,  $\eta_0 = 0.1$  sine wave in the presence of zero viscosity (dashed line) and nonzero viscosity (solid line). The horizontal domain size is 200 with 1000 grid points and the vertical domain size is 100 with 2501 grid points. The addition of viscosity did have an unexpected effect on the resulting dynamics. While the amplitude of the leading crest in Figure 9 is smaller than in the inviscid case, it nevertheless leads the inviscid crest. The role viscosity plays in causing the peak to lead the inviscid case is not yet understood, though examining the dispersion relation with viscous terms retained may explain this behavior.

[56] A practical implication of the role of viscosity is that it acts as a filter on those initial conditions that will initiate observable bores. As seen in section 4.3, increasing the

perturbation wavelength and decreasing the amplitude both act to increase the time over which crest creation occurs. As that time increases, viscous effects become increasingly important in determining whether a bore will develop or whether energy dissipation will prevent bore formation.

#### 4.5. Nonzero Background Stability

[57] In this final section we examine the effects of nonzero stability surrounding the thermal duct. In an effort to more closely model the real atmosphere, we retain the addition of viscosity from section 4.4. Additional runs with zero viscosity (not presented here) demonstrate similar qualitative responses to the results discussed in this section. A stable atmosphere allows for vertical wave propagation and we expect that increasing the background stability will allow initial perturbation energy to leak away from the duct, potentially decreasing or preventing crest creation and bore formation. A number of simulations were performed with  $N_B^2 = 1, 0.5, 0.1, 0.05, 0.01, 0.005, 0.001, 0.0005,$  and  $0.0001$ . Figure 10 displays the results of a  $\lambda = 100$ ,  $\eta_0 = 0.1$  wave for  $N_B^2 = 0.01$  (Figure 10a) and  $N_B^2 = 0.1$  (Figure 10b). The horizontal domain size is 100 with 1000 grid points and the vertical domain size is 100 with 2501 grid points. The dashed lines are the strictly neutral stability case,  $N_B^2 = 0.0$ .

[58] The general trend is that increasing background stability decreases peak amplitudes, with the  $N_B^2 = 0.01$  case being the smallest for which emergent peaks grew and

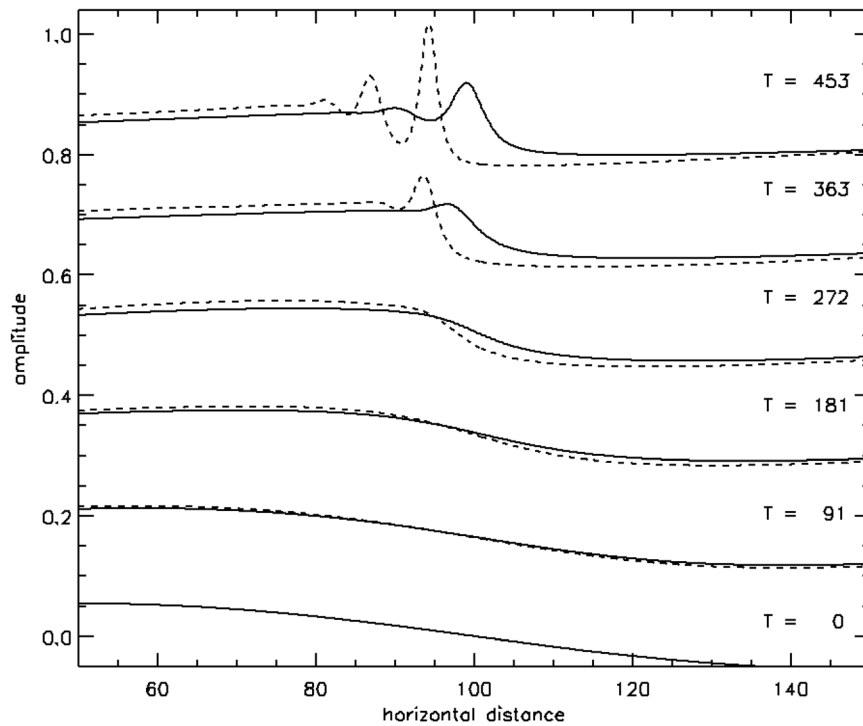


**Figure 9.** Time evolution of a  $\lambda = 200$ ,  $\eta_0 = 0.1$  sinusoidal perturbation in the presence of viscosity. The solid line is the NS solution, and the dashed line is the NS solution in the absence of viscosity.

subsequently decreased in amplitude. As the background stability increases further, the perturbation at the thermal duct decreases to the point at which there is not sufficient energy to drive nonlinear crest creation. This result is shown both in Figure 10b, with  $N_B^2 = 0.1$  and in Figure 11, which is a stationary-frame, partial-domain, false color image (blue is cold, red is hot) of the potential temperature perturbation. The radiation of energy away from the duct is clear from the tilted bands in Figure 11.

[59] The effect of nonzero stability on bore formation was also examined by *Laughman et al.* [2009]. There it was hypothesized that the inhibiting effect of energy radiating away from the duct could be countered by increasing the initial perturbation amplitude, providing a sufficient amplitude over the necessary time scale to allow crest creation. This concept is revisited here, with results presented in Figures 12 and 13. Here the amplitude of the wave in Figure 10b is increased by a factor of three. Both the line plot of Figure 12 and the full-field false color image of Figure 13 demonstrate that the hypothesis of *Laughman et al.* [2009] is correct.

[60] The line plot displays a number of noteworthy features of the  $\eta_0 = 0.3$  case (Figure 12, solid line), especially when contrasted with the  $\eta_0 = 0.1$  case (dashed line) of Figure 11. The first is that the increased amplitude does indeed allow crest creation. Additionally, the peaks occurring for  $\eta_0 = 0.3$  are narrower than previous, smaller amplitude, cases (i.e., Figures 7 and 8), confirming the result of section 4.3 that peak geometry is dependent on the perturbation amplitude. Finally, the amplitudes of the leading peaks decay rapidly, an effect that is partially due to viscous dissipation and possibly due to other dynamic effects such as dispersion.

[61] Figure 13 is a stationary-frame, partial-domain, false color image of the potential temperature field and provides a more complete picture of the resulting dynamics presented in Figure 12. The nonlinear response centered at the duct remains significantly stronger than the radiative response throughout the vertical domain. Furthermore, as early as  $T = 91$  (Figure 13b) the individual peaks form and are seen to modify the long-wave radiation field of Figure 11. As the horizontal scale of the response at the duct decreases,  $k$  increases which, for constant  $N^2$ , results in a smaller  $m$  and larger  $\lambda_z$ . The crests arising in Figure 13 are sufficiently narrow that the  $m^2$  computed by equation (15) in the region above and below the duct is negative, resulting in an evanescent response in that region. The effect of this evanescent perturbation is seen in the modulation of the long-wave radiation beginning at time  $T = 91$  and is clearest at time  $T = 453$ . The question of whether or not a bore can form in the presence of a given background stability may then simply be whether or not the initial perturbation has sufficient amplitude to create crests that are sufficiently narrow as to have a negative  $m^2$  in the region away from the duct and be trapped, though this remains to be examined further.

[62] There is one final concern to address for the case of  $N_B^2 \neq 0.0$ . The vertical boundaries are impermeable, and will necessarily reflect energy back into the domain, potentially leading to unphysical results. This was not an issue in sections 4.1–4.4, where the only effect of these boundaries was the vanishingly small amplitude, fast linear wave response. Here, however, the background stability allows for a significant portion of the initial wave energy to propagate to the boundaries and reflect back to the ducting region. Similar behavior was previously examined and seen to lead to unphysical dynamics [see *Laughman et al.*, 2009].

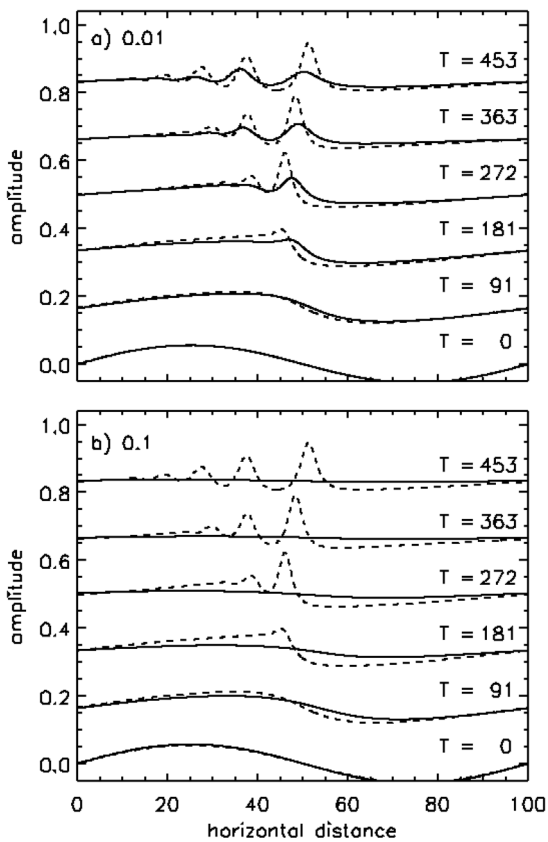


**Figure 10.** Evolution of a  $\lambda = 100$ ,  $\eta_0 = 0.1$  sine wave perturbation in the presence of a nonzero background stability (solid line) and in the presence of a strictly neutral background (dashed line). (a) The background stability is  $N_B^2 = 0.01$ . (b) The background stability is  $N_B^2 = 0.1$ .

Concern that the structure of the response seen in Figures 12 and 13 might somehow be an artifact of this reflection led to the  $N_B^2 = 0.1$ ,  $\eta_0 = 0.3$ ,  $\lambda = 100$  simulation being rerun in a vertical domain that was 8 times larger. The results of that simulation are qualitatively identical to those presented here; the number of peaks, as well as the general shape of the evolution, is the same while actual peak amplitudes vary by as much as 14%. While these results confirm the qualitative validity of the NS model for these environments they also demonstrate that caution must be used in the quantitative application of this model to observation.

## 5. Summary and Conclusions

[63] We have employed two codes solving the Boussinesq Benjamin-Davis-Ono (BDO) equation and the 2-D Boussinesq Navier-Stokes (NS) equations to describe responses to various initial perturbations to an idealized thermal duct at MLT altitudes. Initial perturbations having soliton and sinusoidal forms with varying scales and amplitudes were considered. Also examined were the influences of viscosity and nonzero stability away from the thermal duct. Initial conditions and environments for which the assumptions of the BDO theory are valid yield very good agreement between the BDO and NS solutions extending to late times. However, initial conditions and environments

that violate BDO assumptions to varying degrees lead (as might be expected) to departures of the two solutions in form and with time, with the larger disparities occurring for the more significant violations of BDO assumptions. Viscosity and nonzero stability away from the thermal duct, which are not considered in the simple BDO theory, were likewise found to lead to significant departures of the NS solutions from predictions of BDO theory. Specific differences between the BDO and NS solutions for the various cases considered, summarized below, suggest that applications of BDO theory in interpretations of MLT bore observations may cause errant inferences of bore dynamics and environments, even for relatively simple cases in which only thermal ducting needs to be considered.

[64] For idealized environments, that is, those having zero background stability away from the thermal duct and no viscous dissipation, as well as large spatial scales and weakly nonlinear forcing, BDO solutions are found to closely approximate the NS solutions, even when dispersive effects dominate nonlinear effects. Initial solitons having smaller spatial scales, however, are found to cause increasing departures of NS solutions from BDO predictions. As the initial soliton length scale,  $\lambda = 4\delta/\alpha\eta_0$ , decreases, the NS solution exhibits a smaller amplitude than the BDO solution, a slower phase speed (but still exceeding the maximum linear phase speed,  $c_0$ ), and a dispersive trailing wave train.

[65] Initial soliton-like perturbations (having a soliton shape, but smaller amplitudes than required to balance dispersive and nonlinear effects) yield BDO and NS solutions that remain in close agreement, even for relatively small wavelengths, because the weakly nonlinear assumption of the BDO theory is valid. However, initial perturbations having a soliton shape, but larger amplitudes, yield BDO and NS solutions that differ dramatically because the weakly nonlinear assumption of BDO theory is strongly violated. In these cases, the BDO solutions exhibit higher phase speeds and much more rapid crest creation than is seen in the NS solutions.

[66] We also explored the evolutions of bore responses to initial long-wavelength sinusoidal perturbations in the BDO and NS solutions, given the evidence for such sources in mesospheric bore observations. In these cases, the two solutions agree well where the BDO weakly nonlinear (small-amplitude) assumption is satisfied. As the initial sinusoidal amplitude increases, however, departures of the BDO response from the NS response become more pronounced, with comparable crest spacing in the two solutions, but with higher phase speeds and somewhat faster crest creation occurring in the BDO solutions.

[67] Figure 14 summarizes the observed relationship between crest creation time scale with both amplitude and wavelength for the sinusoidal perturbation. General tendencies seen to occur for both soliton-like and sinusoidal initial perturbations in the BDO and NS solutions can be summarized as follows: (1) The crest creation time scale is proportional to the length scale of the perturbation. (2) The crest creation time scale is inversely proportional to perturbation amplitude. (3) The geometry of the emergent crests is dependent on the perturbation amplitude. (4) The geometry of the emergent crests is independent of the perturbation wavelength. (5) Agreement between the BDO and NS solutions is better for smaller amplitudes and larger

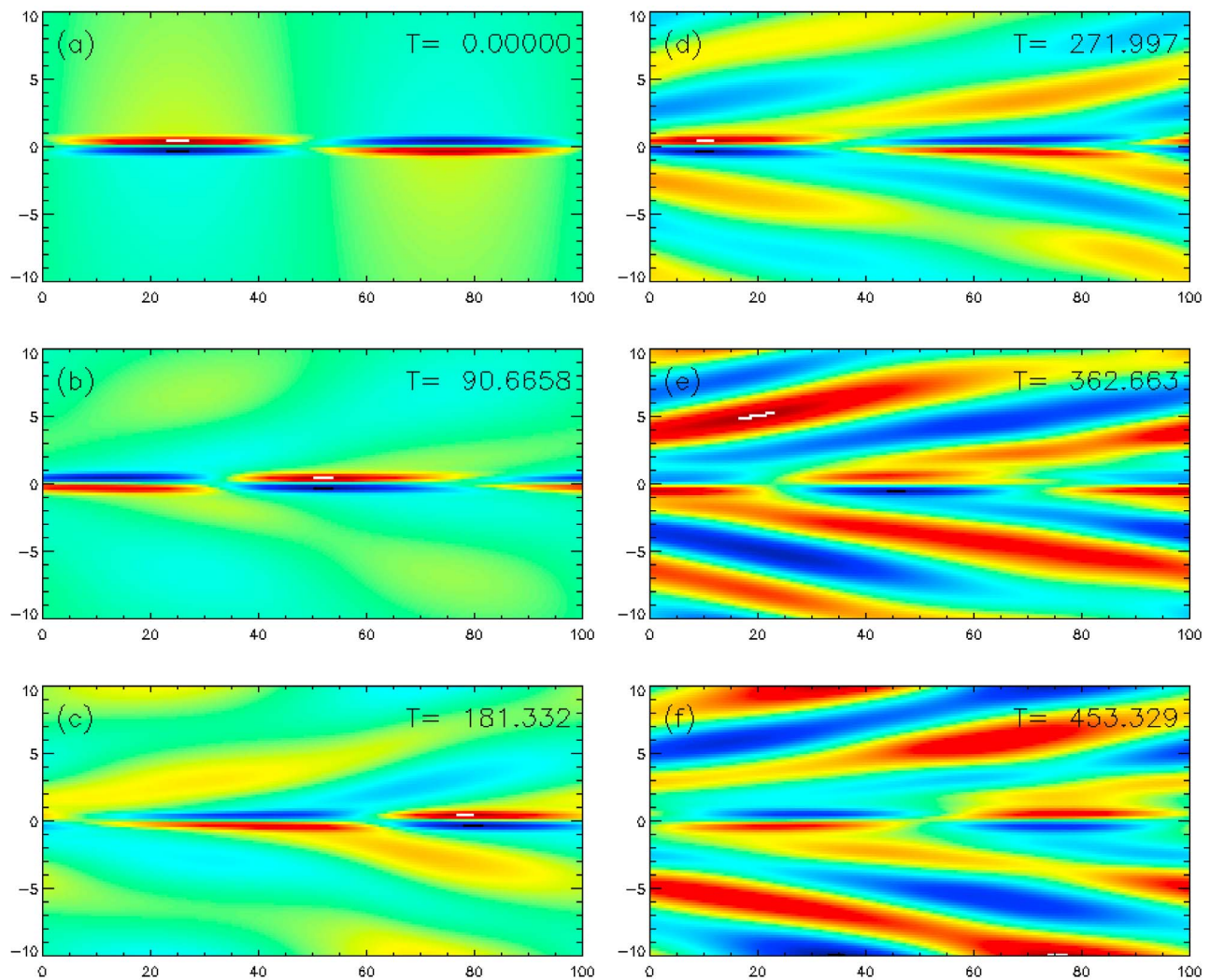


**Figure 11.** (a–f) Evolution of a  $\lambda = 100$ ,  $\eta_0 = 0.1$  sine wave perturbation in the presence of a nonzero background stability  $N_B^2 = 0.1$ . Displayed is the false-colored perturbation potential temperature field at six different times. Blue represents colder, denser fluid, while red represents warmer, less dense fluid.

length scales. (6) Departures of BDO predictions from NS solutions are most pronounced for strongly nonlinear responses. (7) Both BDO predictions and 2-D NS solutions fail to describe bore responses when nonlinearity is sufficiently strong to induce recirculation, overturning, instability, and 3-D turbulence.

[68] Comparisons of NS solutions obtained with negligible and nonnegligible viscosity indicate that rapid viscous dissipation suppresses crest creation and causes the leading peak to advance beyond that of the inviscid case, suggesting that molecular and turbulent dissipation may impact bore evolutions and their interpretations for scales and altitudes at which these effects are nonnegligible. Background stratification that enables an initial sinusoidal perturbation to propagate away from the thermal duct results in rapid depletion of perturbation energy at the thermal duct and weak or no nonlinear steepening and crest creation. Weaker background stratification does not suppress steepening and crest creation entirely, but it does weaken the crests that do arise. Stronger forcing can offset these tendencies to some extent, but nonlinear steepening and crest creation exhibit a

qualitatively different evolution with background stratification than predicted for the same initial perturbation in the absence of background stratification. For large initial perturbation amplitudes, crests may evolve more rapidly with than without background stratification, but they also exhibit smaller crest separations, leading-crest amplitude decay, and bore responses extending to higher and lower altitudes not seen to occur for zero background stratification. We note that similar insights may be drawn from work that extends the scope of the BDO equation to include similar viscous and radiative effects, but that we are not in a position to comment on those extensions since we have not incorporated them into our current BDO model.

[69] To relate our results to bore observations at MLT altitudes, we note that a length scale of 5 km implies a  $\lambda = 100$  perturbation that corresponds to an initial perturbation wavelength of 500 km. Our time scale of  $\sim 19$  s implies initial crest formation after  $\sim 1$  h and a series of  $\sim 3$ – $5$  amplitude-ordered crests over the next 2 h. The separations between crests are variable, with a largest separation of  $\sim 70$  km, a minimum separation of  $\sim 37$  km, and crest FWHM of

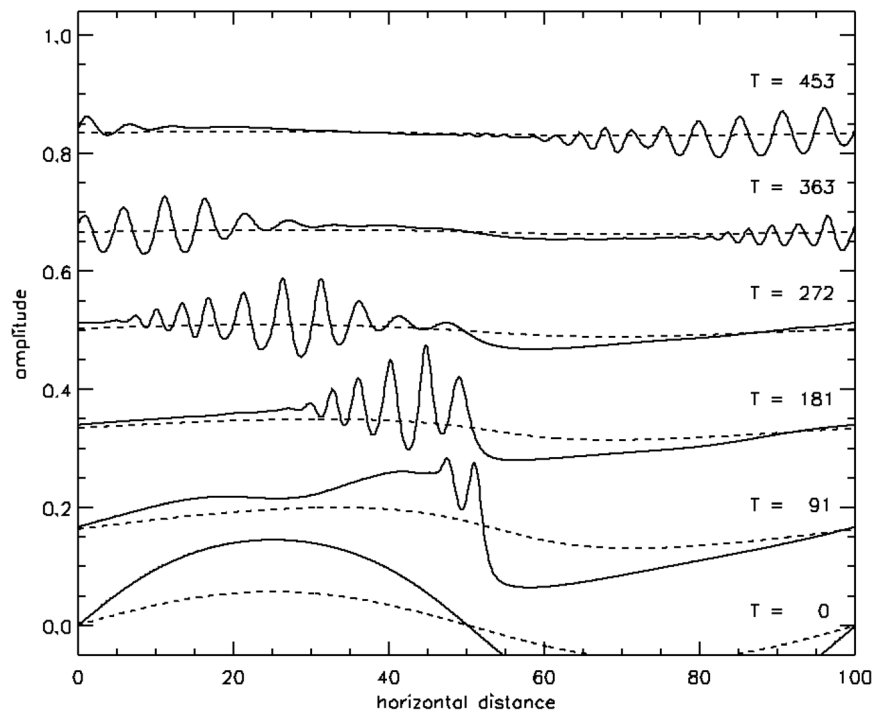


**Figure 12.** Evolution of a  $\lambda = 100$ ,  $\eta_0 = 0.3$  sine wave perturbation (solid line) and a  $\lambda = 100$ ,  $\eta_0 = 0.1$  sine wave perturbation (dashed line) in the presence of a nonzero background stability  $N_B^2 = 0.1$ .

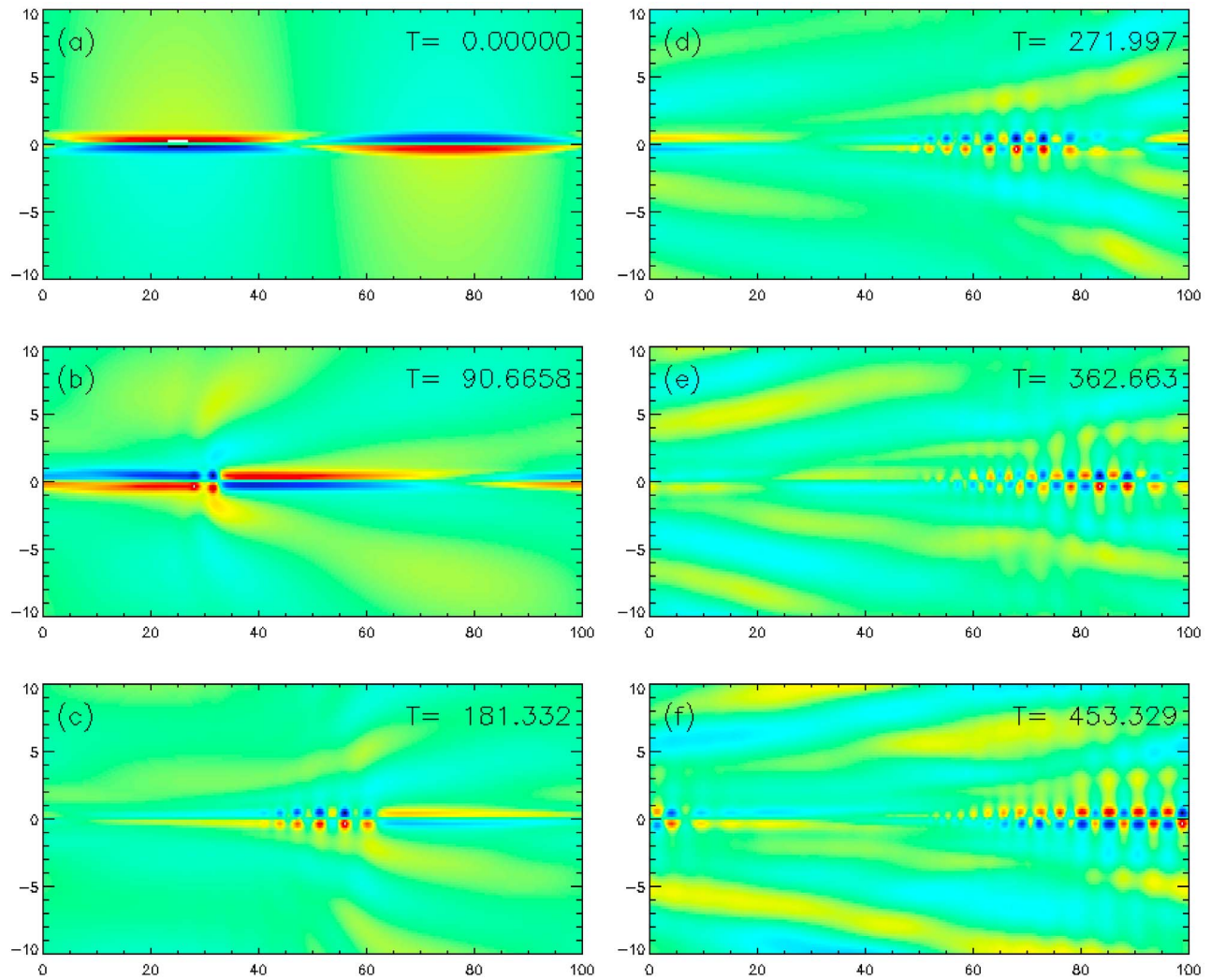


**Figure 13.** (a–f) Evolution of a  $\lambda = 100$ ,  $\eta_0 = 0.3$  sine wave perturbation in the presence of a nonzero background stability  $N_B^2 = 0.1$ . Displayed is the false-colored perturbation potential temperature field at six different times. Blue represents colder, denser fluid, while red represents warmer, less dense fluid.

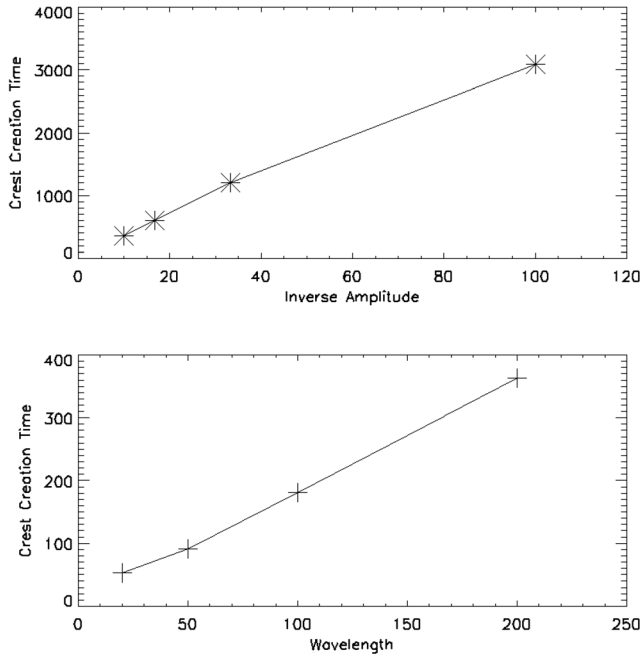


**Figure 14.** Plots of crest creation time scales ( $t_c$ ) for a sinusoidal perturbation as a function of (top) inverse amplitude (asterisks) and (bottom) wavelength (crosses). The solid lines between the data points are drawn for illustration and highlight both the linear relationship between  $1/\eta_0$  and  $t_c$  and the linear relationship between  $\lambda$  and  $t_c$ .

$\sim 20$  km. The corresponding long-wave phase speed is  $\sim 88 \text{ ms}^{-1}$  and the bore phase speed is  $\sim 90\text{--}95 \text{ ms}^{-1}$ . A longer initial wavelength ( $\sim 1000$  km) and a smaller initial amplitude (by  $\sim 2$ ) results in crest creation after  $\sim 3$  h,  $\sim 3\text{--}5$  crests over the next  $\sim 2$  h, and crest FWHM of  $\sim 25$  km. While a duct FWHM of 5 km is on the order of a scale height, these values obtained with the Boussinesq approximation nevertheless compare favorably to observed bores [Medeiros *et al.*, 2001; Batista *et al.*, 2002; Chung *et al.*, 2003; Smith *et al.*, 2003, 2005; She *et al.*, 2004; Fechine *et al.*, 2005, 2009; Shiokawa *et al.*, 2006; Snively and Pasko, 2005; Taylor *et al.*, 1995], though specific bore parameters will depend on the environmental parameters relevant to each observation.

[70] We anticipate that future efforts will address a further quantification of the relationships between environmental parameters and initial conditions and the bore characteristics that arise, including the roles of background stratification and horizontal winds. The initial examination of bores arising owing to Doppler ducting by Laughman *et al.* [2009] demonstrated that these should also be important in the MLT, where much of the small-scale structure in the vertical also has large horizontal scales owing to the dominance of the motion spectrum in many cases by inertia-gravity wave motions. Such future work will make continued use of the BDO equation, both for the comparison it offers the NS predictions as well as the simplified insights it offers to the dynamics.

## Appendix A: BDO Details

[71] This appendix contains additional details regarding the BDO equation, including formulae for computing  $\alpha$ ,  $\delta$ ,

$c_0$ , and  $\phi(z)$ . Recall that  $\eta(x, z, t)$  can be decomposed into two functions,

$$\eta(x, z, t) = A(x, t) \phi(z). \quad (\text{A1})$$

The modal function,  $\phi(z)$ , and the long-wave phase speed,  $c_0$ , are the solutions of the non-Boussinesq modal equation [Ono, 1975],

$$\frac{d}{dz} \left\{ \rho_0(z) \frac{d\phi(z)}{dz} \right\} - \frac{g}{c_0^2} \frac{d\rho_0(z)}{dz} \phi(z) = 0, \quad (\text{A2})$$

where  $g$  is acceleration due to gravity and  $\rho_0(z)$  is the unperturbed density profile. The unperturbed density is defined as

$$\rho_0(z) = \begin{cases} \rho_0 (= \text{const}), & |z| > h \\ \rho_0(z), & |z| \leq h \end{cases}. \quad (\text{A3})$$

Using the definition for the buoyancy frequency,

$$N^2(z) = -\frac{g}{\rho_0(z)} \frac{d\rho_0(z)}{dz}, \quad (\text{A4})$$

and the Boussinesq approximation we rewrite equation (A2) as

$$\frac{d^2\phi(z)}{dz^2} + \frac{N^2(z)}{c_0^2} \phi(z) = 0, \quad (\text{A5})$$

which is an eigenvalue problem that can then be solved for the eigenvalue  $c_0$  and corresponding eigenfunction  $\phi(z)$ . There are three conditions imposed on  $\phi(z)$ :  $\phi(0) = 0$ ,  $\phi(h) = 1$ , and  $\phi'(h) = 0$  [Ono, 1975]. We note that the lowest-order eigenfunction corresponds to the largest eigenvalue  $c_0$ , and as it is this lowest mode that dominates observation we, like some past authors, restrict our study to this the lowest mode.

[72] Formulae for computing  $\alpha$  and  $\delta$  can be found in the work of Grimshaw [1980] and rewritten subject to inviscid and incompressible approximations, yielding

$$I\alpha = 3 \int_0^\infty \rho_0 c_0^2 \left( \frac{\partial\phi(z)}{\partial z} \right)^3 dz, \quad (\text{A6a})$$

$$I\delta = \lim_{z \rightarrow \infty} c^2(\rho_0 \phi^2), \quad (\text{A6b})$$

$$I = 2 \int_0^\infty \rho_0 c_0 \left( \frac{\partial\phi(z)}{\partial z} \right)^2 dz. \quad (\text{A6c})$$

With  $\alpha$ ,  $\delta$ , and  $c_0$  defined, the evolution equation for  $A(x, t)$  can be written as

$$\frac{\partial A}{\partial t} + c_0 \frac{\partial A}{\partial x} + \alpha A \frac{\partial A}{\partial x} + \delta \frac{\partial^2}{\partial x^2} H(A) = 0, \quad (\text{A7})$$

which is the BDO equation.  $H(A)$  is the Hilbert transform of  $A$ , defined as

$$H[A(x)] = \frac{1}{\pi} \int_{-\infty}^\infty \frac{A(x')}{x' - x} dx'. \quad (\text{A8})$$

This definition is used by authors such as *Christie* [1989], but is not a uniformly accepted definition, and other authors such as *Ono* [1975] define  $H(A)$  as  $-H(A)$ . This sign ambiguity also leads some authors to compute  $\delta$  in equation (A6) as  $-\delta$ .

[73] As the limits of integration in equation (A6) indicate, there are two regions to consider when using the BDO equation. Figure 1b depicts both the inner region where the density changes with altitude, and the outer region where the density is a constant. Fluid displacement in the inner region,  $[0, h]$ , is given by equation (A1), while displacement in the outer region,  $[h, \infty]$ , can be computed from

$$\eta(x, z, t) = \int_{-\infty}^{\infty} F(A) \exp[-ikx - |k|(z - h)] dk, \quad (\text{A9})$$

where  $F$  is a linear operator defined by

$$F(A) = \frac{1}{2\pi} \int_{-\infty}^{\infty} A(x, t) \exp(ikx) dx. \quad (\text{A10})$$

We now illustrate the above theory for the  $\text{sech}^2$  duct, which is convenient and insightful owing to its analytic nature. The  $\text{sech}^2$  stability profile corresponds to a hyperbolic tangent density profile. Again, we examine the upper half plane as depicted in Figure 1b.

[74] The  $\text{sech}^2$  profile also has the property of asymptotically approaching a value of 1 as  $z$  tends to infinity. In order to strictly satisfy the definition given by equation (A3), this would define an  $h$  for the inner region that is infinitely large. A more useful treatment is to instead define  $h$  by  $N^2(z) = \text{sech}^2(z/h)$  [*Benjamin*, 1967; *Christie*, 1989]. Substituting  $N^2(z) = \text{sech}^2(z/h)$  into equations (5) and (6) yields  $c_0 = 2^{-1/2} N_0 h$ ,  $\alpha = 6/5 c_0/h$ , and  $\delta = 3/4 c_0 h$ . These are the analytically obtained values presented in Table 1 of section 3.

[75] Substituting these values into equation (A7) then yields the correct evolution equation for finite-amplitude long-wave perturbations to the fluid field in the presence of a  $\text{sech}^2$  density stratification.

[76] **Acknowledgments.** This research was supported by NSF grants ATM-0924802, ATM-0314060, and ATM-0836407. The authors also thank three anonymous reviewers for their comments, corrections, and insights.

## References

- Airy, G. B. (1845), *Tides and Waves*, B. Fellowes, London.
- Batista, P. P., B. R. Clemesha, D. M. Simonich, M. J. Taylor, H. Takahashi, D. Gobbi, I. S. Batista, R. A. Buriti, and A. F. de Medeiros (2002), Simultaneous lidar observation of a sporadic sodium layer: A "wall" event in the OH and OI5577 airglow images and the meteor winds, *J. Atmos. Sol. Terr. Phys.*, *64*, 1327–1335, doi:10.1016/S1364-6826(02)00116-5.
- Benjamin, T. B. (1967), Internal wave of permanent form in fluids of great depth, *J. Fluid Mech.*, *29*, 559–592, doi:10.1017/S002211206700103X.
- Christie, D. R. (1989), Long nonlinear waves in the lower atmosphere, *J. Atmos. Sci.*, *46*, 1462–1490, doi:10.1175/1520-0469(1989)046<1462:LNWITL>2.0.CO;2.
- Chung, J.-K., Y. H. Kim, and Y.-I. Won (2003), Observations of mesospheric waves with an all-sky camera in Korean Peninsula, *Adv. Space Res.*, *32*(5), 825–830, doi:10.1016/S0273-1177(03)00414-9.
- Davis, R. E., and A. Arcivos (1967), Solitary internal waves in deep water, *J. Fluid Mech.*, *29*, 593–607, doi:10.1017/S0022112067001041.
- Dewan, E. M., and R. H. Picard (1998), Mesospheric bores, *J. Geophys. Res.*, *103*, 6295–6305, doi:10.1029/97JD02498.
- Dewan, E. M., and R. H. Picard (2001), On the origin of mesospheric bores, *J. Geophys. Res.*, *106*, 2921–2927, doi:10.1029/2000JD900697.
- Fechine, J., A. F. Medeiros, R. A. Buriti, H. Takahashi, and D. Gobbi (2005), Mesospheric bore events in the equatorial middle atmosphere, *J. Atmos. Sol. Terr. Phys.*, *67*, 1774–1778, doi:10.1016/j.jastp.2005.04.006.
- Fechine, J., et al. (2009), First observation of an undular mesospheric bore in a Doppler duct, *Ann. Geophys.*, *27*, 1399–1406, doi:10.5194/angeo-27-1399-2009.
- Fritts, D. C., C. Bizon, J. A. Werne, and C. K. Meyer (2003), Layering accompanying turbulence generation due to shear instability and gravity wave breaking, *J. Geophys. Res.*, *108*(D8), 8452, doi:10.1029/2002JD002406.
- Fritts, D. C., S. L. Vadas, K. Wan, and J. A. Werne (2006), Mean and variable forcing of the middle atmosphere by gravity waves, *J. Atmos. Sol. Terr. Phys.*, *68*, 247–265, doi:10.1016/j.jastp.2005.04.010.
- Fritts, D. C., L. Wang, J. Werne, T. Lund, and K. Wan (2009a), Gravity wave instability dynamics at high Reynolds numbers, 1: Wave field evolution at large amplitudes and high frequencies, *J. Atmos. Sci.*, *66*, 1126–1148, doi:10.1175/2008JAS2726.1.
- Fritts, D. C., L. Wang, J. Werne, T. Lund, and K. Wan (2009b), Gravity wave instability dynamics at high Reynolds numbers, 2: Turbulence evolution, structure, and anisotropy, *J. Atmos. Sci.*, *66*, 1149–1171, doi:10.1175/2008JAS2727.1.
- Grimshaw, R. (1980), Solitary waves in a compressible fluid, *Pure Appl. Geophys.*, *119*, 780–797, doi:10.1007/BF01131255.
- Hammack, J. L., and H. Segur (1974), The Korteweg-de Vries equation and water waves. Part 2: Comparison with experiments, *J. Fluid Mech.*, *65*, 289–314, doi:10.1017/S002211207400139X.
- Koop, C. G., and G. Butler (1981), An investigation of internal solitary waves in a two-fluid system, *J. Fluid Mech.*, *112*, 225–251, doi:10.1017/S0022112081000372.
- Korteweg, D. J., and F. de Vries (1895), On the change of form of long waves advancing in a rectangular canal, and on a new type of long stationary waves, *Philos. Mag.*, *39–40*, 421–444.
- Lamb, H. (1932), *Hydrodynamics*, 6th ed., Cambridge Univ. Press, New York.
- Laughman, B. (2009), Numerical modeling of mesospheric bores, Ph.D. thesis, Univ. of Colo. at Boulder, Boulder.
- Laughman, B., D. C. Fritts, and J. Werne (2009), Numerical simulation of bore generation and morphology in thermal and Doppler ducts, *Ann. Geophys.*, *27*, 511–523.
- Lighthill, J. (1978), *Waves in Fluids*, Cambridge Univ. Press, New York.
- Maslowe, S. A., and L. G. Redekopp (1980), Long nonlinear waves in stratified shear flows, *J. Fluid Mech.*, *101*, 321–348, doi:10.1017/S0022112080001681.
- Medeiros, A. F., M. J. Taylor, H. Takahashi, P. P. Batista, and D. Gobbi (2001), An unusual airglow wave event observed at Cachoeira Paulista 23°S, *Adv. Space Res.*, *27*(10), 1749–1754, doi:10.1016/S0273-1177(01)00317-9.
- Miles, J. W. (1981), The Korteweg-de Vries equation: A historical essay, *J. Fluid Mech.*, *106*, 131–147, doi:10.1017/S0022112081001559.
- Ono, H. (1975), Algebraic solitary wave in stratified fluids, *J. Phys. Soc. Jpn.*, *39*, 1082–1091, doi:10.1143/JPSJ.39.1082.
- Porter, A., and N. Smyth (2002), Modelling the morning glory of the Gulf of Carpentaria, *J. Fluid Mech.*, *454*, 1–20, doi:10.1017/S0022112001007455.
- Rayleigh, Lord (J. W. Strutt) (1908), Note on tidal bores, *Proc. R. Soc. London, Ser. A*, *81*, 448–449. (Reprinted in *Scientific Papers by Lord Rayleigh*, vol. 5, Pap. 333, p. 495, Dover, Mineola, N. Y., 1964.)
- Seyler, C. E. (2005), Internal wave and undular bores in mesospheric inversion layers, *J. Geophys. Res.*, *110*, D09S05, doi:10.1029/2004JD004685.
- She, C. Y., T. Li, B. P. Williams, T. Yuan, and R. H. Picard (2004), Concurrent OH imager and sodium temperature/wind lidar observation of a mesopause region undular bore event over Fort Collins/Platteville, Colorado, *J. Geophys. Res.*, *109*, D22107, doi:10.1029/2004JD004742.
- Shiokawa, K., S. Suzuki, Y. Otsuka, T. Ogawa, T. Nakamura, M. G. Mlynecak, and M. J. Russell III (2006), A multi-instrument measurement of a mesospheric front-like structure at the equator, *J. Meteorol. Soc. Jpn.*, *84A*, 305–316, doi:10.2151/jmsj.84A.305.
- Smith, S. M., M. J. Taylor, G. R. Swenson, C. Y. She, W. Hocking, J. Baumgardner, and M. Mendillo (2003), A multidagnostic investigation of the mesospheric bore phenomenon, *J. Geophys. Res.*, *108*(A2), 1083, doi:10.1029/2002JA009500.
- Smith, S., M. J. Friedman, S. Raizada, C. Tepley, J. Baumgardner, and M. Mendillo (2005), Evidence of mesospheric bore formation from a breaking gravity wave event: Simultaneous imaging and lidar measurements, *J. Atmos. Sol. Terr. Phys.*, *67*, 345–356, doi:10.1016/j.jastp.2004.11.008.

- Snively, J. B., and V. P. Pasko (2005), Antiphase OH and OI airglow emissions induced by a short-period ducted gravity wave, *Geophys. Res. Lett.*, *32*, L08808, doi:10.1029/2004GL022221.
- Spalart, P. R., R. D. Moser, and M. M. Rogers (1991), Spectral methods for the Navier-Stokes equations with one infinite and two periodic directions, *J. Comput. Phys.*, *96*, 297–324, doi:10.1016/0021-9991(91)90238-G.
- Taylor, M. J., D. N. Turnbull, and R. P. Lowe (1995), Spectrometric and imaging measurements of a spectacular gravity wave event observed during the ALOHA-93 campaign, *Geophys. Res. Lett.*, *22*, 2849–2852, doi:10.1029/95GL02948.
- Werne, J. A., and D. C. Fritts (1999), Stratified shear turbulence: Evolution and statistics, *Geophys. Res. Lett.*, *26*, 439–442, doi:10.1029/1999GL900022.
- Werne, J. A., and D. C. Fritts (2001), Anisotropy in a stratified shear layer, *Phys. Chem. Earth*, *26*, 263–268.
- 
- D. C. Fritts, B. Laughman, and J. Werne, CoRA Division, NorthWest Research Associates, 3380 Mitchell Ln., Boulder, CO 80301, USA. (laughman@cora.nwra.com)